Experimental Validation on the ID31 Beamline

Dehaeze Thomas

February 20, 2025

Contents

To proceed with the full validation of the Nano Active Stabilization System (NASS), the nano-hexapod was mounted on top of the micro-station on ID31, as illustrated in figure 1. This section presents a comprehensive experimental evaluation of the complete system's performance on the ID31 beamline, focusing on its ability to maintain precise sample positioning under various experimental conditions.

Initially, the project planned to develop a long-stroke ($\approx 1\,cm^3$) 5-DoF metrology system to measure the sample position relative to the granite base. However, the complexity of this development prevented its completion before the experimental testing phase on ID31. To validate the nano-hexapod and its associated control architecture, an alternative short-stroke ($\approx 100\,\mu m^3$) metrology system was developed, which is presented in Section 1.

Then, several key aspects of the system validation are examined. Section 2 analyzes the identified dynamics of the nano-hexapod mounted on the micro-station under various experimental conditions, including different payload masses and rotational velocities. These measurements were compared with predictions from the multi-body model to verify its accuracy and applicability to control design.

Sections 3 and 4 focus on the implementation and validation of the HAC-LAC control architecture. First, Section 3 demonstrates the application of decentralized Integral Force Feedback for robust active damping of the nano-hexapod suspension modes. This is followed in Section 4 by the implementation of the high authority controller, which addresses low-frequency disturbances and completes the control system design.

Finally, Section 5 evaluates the NASS's positioning performances through a comprehensive series of experiments that mirror typical scientific applications. These include tomography scans at various speeds and with different payload masses, reflectivity measurements, and combined motion sequences that test the system's full capabilities.

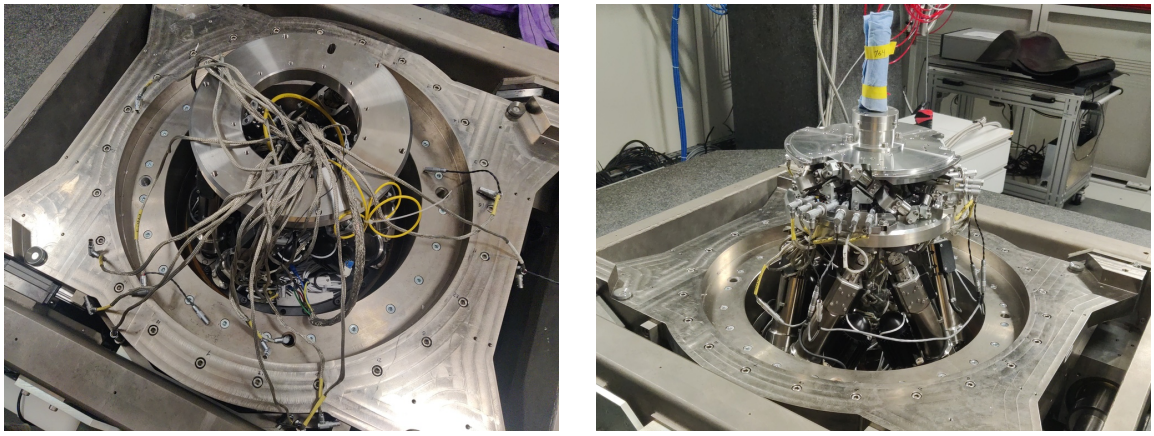

(a) Micro-station and nano-hexapod cables **(b)** Nano-hexapod fixed on top of the micro-station

Figure 1: Picture of the micro-station without the nano-hexapod (a) and with the nano-hexapod (b)

1 Short Stroke Metrology System

The control of the nano-hexapod requires an external metrology system that measures the relative position of the nano-hexapod top platform with respect to the granite. As a long-stroke ($\approx 1\,cm^3$) metrology system was not yet developed, a stroke stroke ($\approx 100\,\mu m^3$) was used instead to validate the nano-hexapod control.

The first considered option was to use the "Spindle error analyzer" shown in Figure 1.1a. This system comprises 5 capacitive sensors facing two reference spheres. However, as the gap between the capacitive sensors and the spheres is very small[1], the risk of damaging the spheres and the capacitive sensors is too high.

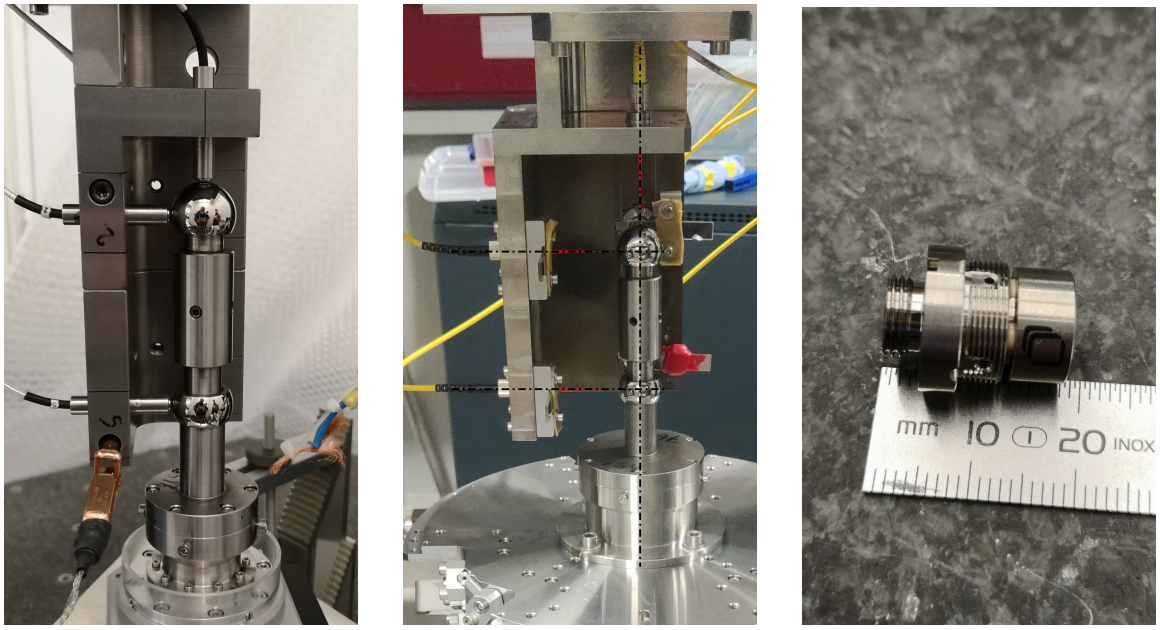

(a) Capacitive Sensors **(b)** Short-Stroke metrology **(c)** Interferometer head

Figure 1.1: Short stroke metrology system used to measure the sample position with respect to the granite in 5DoF. The system is based on a "Spindle error analyzer" (a), but the capacitive sensors are replaced with fibered interferometers (b). The interferometer heads are shown in (c)

Instead of using capacitive sensors, 5 fibered interferometers were used in a similar manner (Figure 1.1b). At the end of each fiber, a sensor head[2] (Figure 1.1c) is used, which consists of a lens precisely positioned with respect to the fiber's end. The lens focuses the light on the surface of the sphere, such that the reflected light comes back into the fiber and produces an interference. In this way, the gap

[1] Depending on the measuring range, gap can range from $\approx 1\,\mu m$ to $\approx 100\,\mu m$.
[2] M12/F40 model from Attocube.

between the head and the reference sphere is much larger (here around $40\,mm$), thereby removing the risk of collision.

Nevertheless, the metrology system still has a limited measurement range because of the limited angular acceptance of the fibered interferometers. Indeed, when the spheres are moving perpendicularly to the beam axis, the reflected light does not coincide with the incident light, and above some perpendicular displacement, the reflected light does not come back into the fiber, and no interference is produced.

1.1 Metrology Kinematics

The proposed short-stroke metrology system is schematized in Figure 1.2. The point of interest is indicated by the blue frame $\{B\}$, which is located $H = 150\,mm$ above the nano-hexapod's top platform. The spheres have a diameter $d = 25.4\,mm$, and the indicated dimensions are $l_1 = 60\,mm$ and $l_2 = 16.2\,mm$. To compute the pose of $\{B\}$ with respect to the granite (i.e. with respect to the fixed interferometer heads), the measured (small) displacements $[d_1,\ d_2,\ d_3,\ d_4,\ d_5]$ by the interferometers are first written as a function of the (small) linear and angular motion of the $\{B\}$ frame $[D_x,\ D_y,\ D_z,\ R_x,\ R_y]$ (1.1).

$$d_1 = D_y - l_2 R_x, \quad d_2 = D_y + l_1 R_x, \quad d_3 = -D_x - l_2 R_y, \quad d_4 = -D_x + l_1 R_y, \quad d_5 = -D_z \tag{1.1}$$

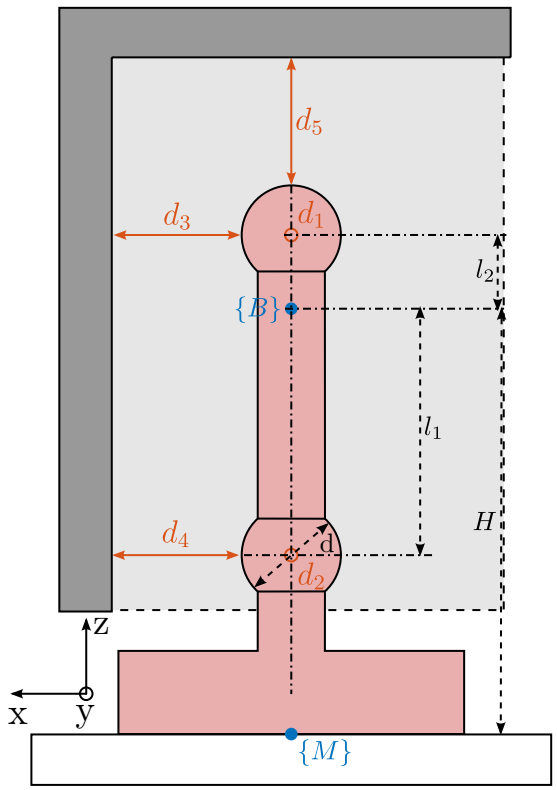

Figure 1.2: Schematic of the measurement system. The measured distances are indicated by red arrows.

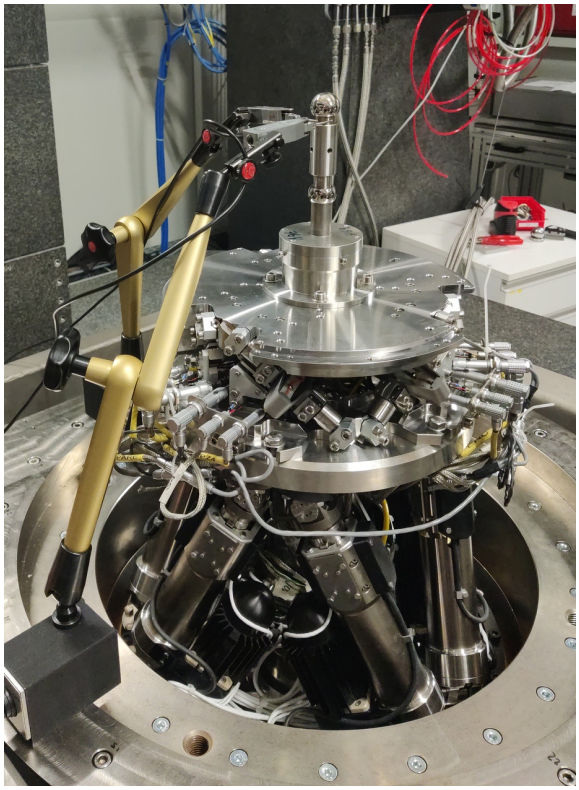

Figure 1.3: The top sphere is aligned with the rotation axis of the spindle using two probes.

The five equations (1.1) can be written in matrix form, and then inverted to have the pose of the $\{B\}$ frame as a linear combination of the measured five distances by the interferometers (1.2).

$$\begin{bmatrix} D_x \\ D_y \\ D_z \\ R_x \\ R_y \end{bmatrix} = \underbrace{\begin{bmatrix} 0 & 1 & 0 & -l_2 & 0 \\ 0 & 1 & 0 & l_1 & 0 \\ -1 & 0 & 0 & 0 & -l_2 \\ -1 & 0 & 0 & 0 & l_1 \\ 0 & 0 & -1 & 0 & 0 \end{bmatrix}^{-1}}_{\boldsymbol{J_d}} \cdot \begin{bmatrix} d_1 \\ d_2 \\ d_3 \\ d_4 \\ d_5 \end{bmatrix} \tag{1.2}$$

1.2 Rough alignment of the reference spheres

The two reference spheres must be well aligned with the rotation axis of the spindle. To achieve this, two measuring probes were used as shown in Figure 1.3.

To not damage the sensitive sphere surface, the probes are instead positioned on the cylinder on which the sphere is mounted. The probes are first fixed to the bottom (fixed) cylinder to align the first sphere with the spindle axis. The probes are then fixed to the top (adjustable) cylinder, and the same alignment is performed.

With this setup, the alignment accuracy of both spheres with the spindle axis was expected to around $10\,\mu m$. The accuracy was probably limited by the poor coaxiality between the cylinders and the spheres. However, this first alignment should be sufficient to position the two sphere within the acceptance range of the interferometers.

1.3 Tip-Tilt adjustment of the interferometers

The short-stroke metrology system was placed on top of the main granite using granite blocs (Figure 1.4). Granite is used for its good mechanical and thermal stability.

The interferometer beams must be placed with respect to the two reference spheres as close as possible to the ideal case shown in Figure 1.2. Therefore, their positions and angles must be well adjusted with respect to the two spheres. First, the vertical positions of the spheres is adjusted using the micro-hexapod to match the heights of the interferometers. Then, the horizontal position of the gantry is adjusted such that the intensity of the light reflected back in the fiber of the top interferometer is maximized. This is equivalent as to optimize the perpendicularity between the interferometer beam and the sphere surface (i.e. the concentricity between the top beam and the sphere center).

The lateral sensor heads (i.e. all except the top one) were each fixed to a custom tip-tilt adjustment mechanism. This allows them to be individually oriented so that they all point to the spheres' center (i.e. perpendicular to the sphere surface). This is achieved by maximizing the intensity of the reflected light of each interferometer.

After the alignment procedure, the top interferometer should coincide with the spindle axis, and the lateral interferometers should all be in the horizontal plane and intersect the centers of the spheres.

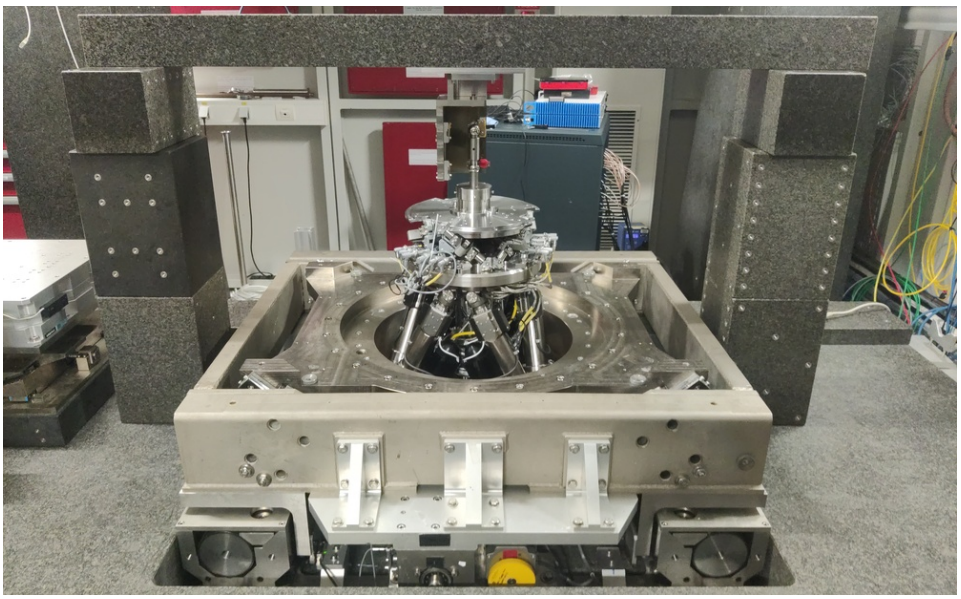

Figure 1.4: Granite gantry used to fix the short-stroke metrology system

1.4 Fine Alignment of reference spheres using interferometers

Thanks to the first alignment of the two reference spheres with the spindle axis (Section 1.2) and to the fine adjustment of the interferometer orientations (Section 1.3), the spindle can perform complete rotations while still having interference for all five interferometers. Therefore, this metrology can be used to better align the axis defined by the centers of the two spheres with the spindle axis.

The alignment process requires few iterations. First, the spindle is scanned, and alignment errors are recorded. From the errors, the motion of the micro-hexapod to better align the spheres with the spindle axis is computed and the micro-hexapod is positioned accordingly. Then, the spindle is scanned again, and new alignment errors are recorded.

This iterative process is first performed for angular errors (Figure 1.5a) and then for lateral errors (Figure 1.5b). The remaining errors after alignment are in the order of $\pm 5\,\mu$rad in R_x and R_y orientations, $\pm 1\,\mu m$ in D_x and D_y directions, and less than $0.1\,\mu m$ vertically.

1.5 Estimated measurement volume

Because the interferometers point to spheres and not flat surfaces, the lateral acceptance is limited. To estimate the metrology acceptance, the micro-hexapod was used to perform three accurate scans of $\pm 1\,mm$, respectively along the x, y and z axes. During these scans, the 5 interferometers are recorded individually, and the ranges in which each interferometer had enough coupling efficiency to be able to measure the displacement were estimated. Results are summarized in Table 1.1. The obtained lateral acceptance for pure displacements in any direction is estimated to be around $+/-0.5\,mm$, which is enough for the current application as it is well above the micro-station errors to be actively corrected by the NASS.

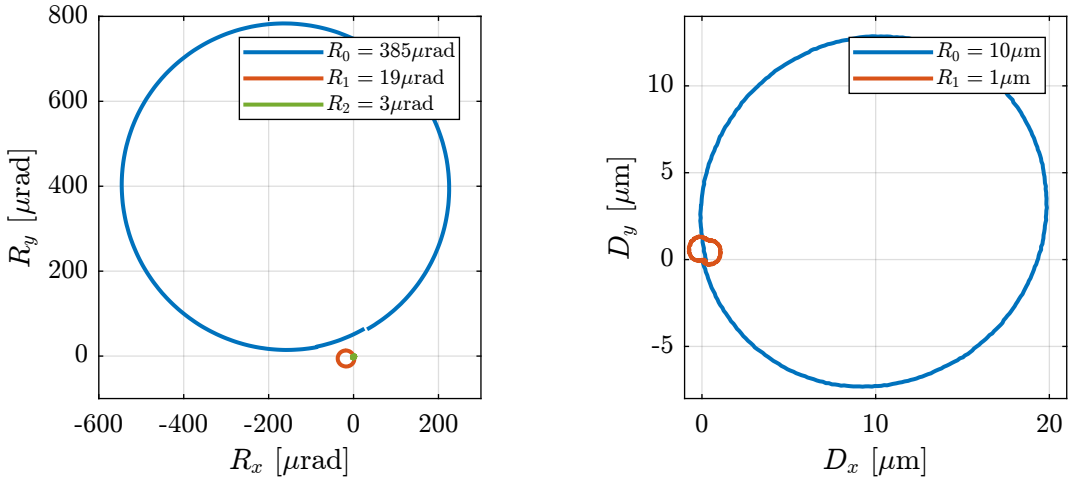

(a) Angular alignment

(b) Lateral alignment

Figure 1.5: Measured angular (a) and lateral (b) errors during full spindle rotation. Between two rotations, the micro-hexapod is adjusted to better align the two spheres with the rotation axis.

Table 1.1: Estimated measurement range for each interferometer, and for three different directions.

	D_x	D_y	D_z
d_1 (y)	$1.0\,mm$	$> 2\,mm$	$1.35\,mm$
d_2 (y)	$0.8\,mm$	$> 2\,mm$	$1.01\,mm$
d_3 (x)	$> 2\,mm$	$1.06\,mm$	$1.38\,mm$
d_4 (x)	$> 2\,mm$	$0.99\,mm$	$0.94\,mm$
d_5 (z)	$1.33\,mm$	$1.06\,mm$	$> 2\,mm$

1.6 Estimated measurement errors

When using the NASS, the accuracy of the sample positioning is determined by the accuracy of the external metrology. However, the validation of the nano-hexapod, the associated instrumentation, and the control architecture is independent of the accuracy of the metrology system. Only the bandwidth and noise characteristics of the external metrology are important. However, some elements that affect the accuracy of the metrology system are discussed here.

First, the "metrology kinematics" (discussed in Section 1.1) is only approximate (i.e. valid for small displacements). This can be easily seen when performing lateral $[D_x,\ D_y]$ scans using the micro-hexapod while recording the vertical interferometer (Figure 1.6a). As the top interferometer points to a sphere and not to a plane, lateral motion of the sphere is seen as a vertical motion by the top interferometer.

Then, the reference spheres have some deviations relative to an ideal sphere [3]. These sphere are originally intended for use with capacitive sensors that integrate shape errors over large surfaces. When using interferometers, the size of the "light spot" on the sphere surface is a circle with a diameter approximately equal to $50\,\mu m$, and therefore the measurement is more sensitive to shape errors with small features.

As the light from the interferometer travels through air (as opposed to being in vacuum), the measured distance is sensitive to any variation in the refractive index of the air. Therefore, any variation in air temperature, pressure or humidity will induce measurement errors. For instance, for a measurement length of $40\,mm$, a temperature variation of $0.1\,^oC$ (which is typical for the ID31 experimental hutch) induces errors in the distance measurement of $\approx 4\,nm$.

Interferometers are also affected by noise [1]. The effect of noise on the translation and rotation measurements is estimated in Figure 1.6b.

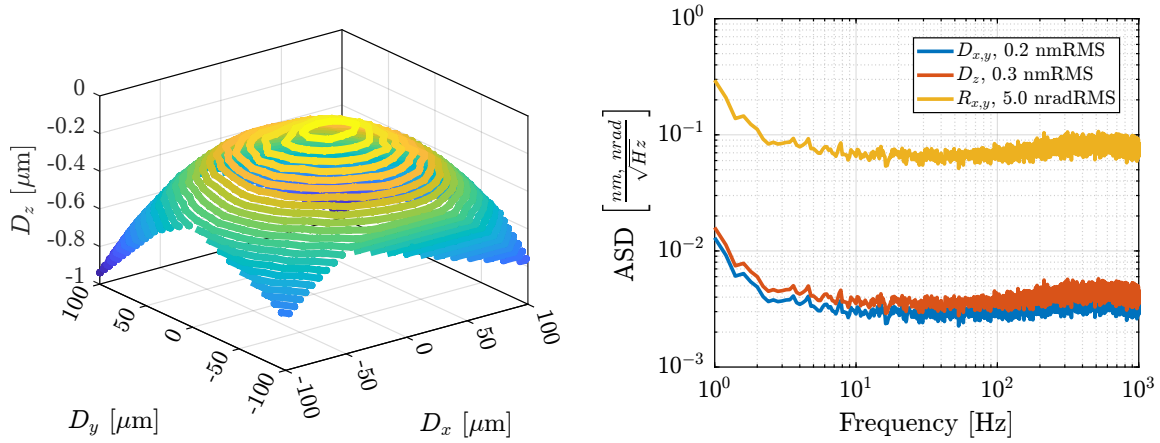

(a) Z measurement during an XY mapping

(b) Interferometer noise

Figure 1.6: Estimated measurement errors of the metrology. Cross-coupling between lateral motion and vertical measurement is shown in (a). The effect of interferometer noise on the measured translations and rotations is shown in (b).

[3] The roundness of the spheres is specified at $50\,nm$.

2 Open Loop Plant

The NASS plant is schematically illustrated in Figure 2.1. The input $\boldsymbol{u} = [u_1,\ u_2,\ u_3,\ u_4,\ u_5,\ u_6]$ is the command signal, which corresponds to the voltages generated for each piezoelectric actuator. After amplification, the voltages across the piezoelectric stack actuators are $\boldsymbol{V}_a = [V_{a1},\ V_{a2},\ V_{a3},\ V_{a4},\ V_{a5},\ V_{a6}]$.

From the setpoint of micro-station stages (r_{D_y} for the translation stage, r_{R_y} for the tilt stage and r_{R_z} for the spindle), the reference pose of the sample $\boldsymbol{r}_{\mathcal{X}}$ is computed using the micro-station's kinematics. The sample's position $\boldsymbol{y}_{\mathcal{X}} = [D_x,\ D_y,\ D_z,\ R_x,\ R_y,\ R_z]$ is measured using multiple sensors. First, the five interferometers $\boldsymbol{d} = [d_1,\ d_2,\ d_3,\ d_4,\ d_5]$ are used to measure the $[D_x,\ D_y,\ D_z,\ R_x,\ R_y]$ degrees of freedom of the sample. The R_z position of the sample is computed from the spindle's setpoint r_{R_z} and from the 6 encoders $\boldsymbol{d}_e$ integrated in the nano-hexapod.

The sample's position $\boldsymbol{y}_{\mathcal{X}}$ is compared to the reference position $\boldsymbol{r}_{\mathcal{X}}$ to compute the position error in the frame of the (rotating) nano-hexapod $\boldsymbol{\epsilon}\boldsymbol{\mathcal{X}} = [\epsilon_{D_x},\ \epsilon_{D_y},\ \epsilon_{D_z},\ \epsilon_{R_x},\ \epsilon_{R_y},\ \epsilon_{R_z}]$. Finally, the Jacobian matrix $\boldsymbol{J}$ of the nano-hexapod is used to map $\boldsymbol{\epsilon}\boldsymbol{\mathcal{X}}$ in the frame of the nano-hexapod struts $\boldsymbol{\epsilon}\boldsymbol{\mathcal{L}} = [\epsilon_{\mathcal{L}_1},\ \epsilon_{\mathcal{L}_2},\ \epsilon_{\mathcal{L}_3},\ \epsilon_{\mathcal{L}_4},\ \epsilon_{\mathcal{L}_5},\ \epsilon_{\mathcal{L}_6}]$.

Voltages generated by the force sensor piezoelectric stacks $\boldsymbol{V}_s = [V_{s1},\ V_{s2},\ V_{s3},\ V_{s4},\ V_{s5},\ V_{s6}]$ will be used for active damping.

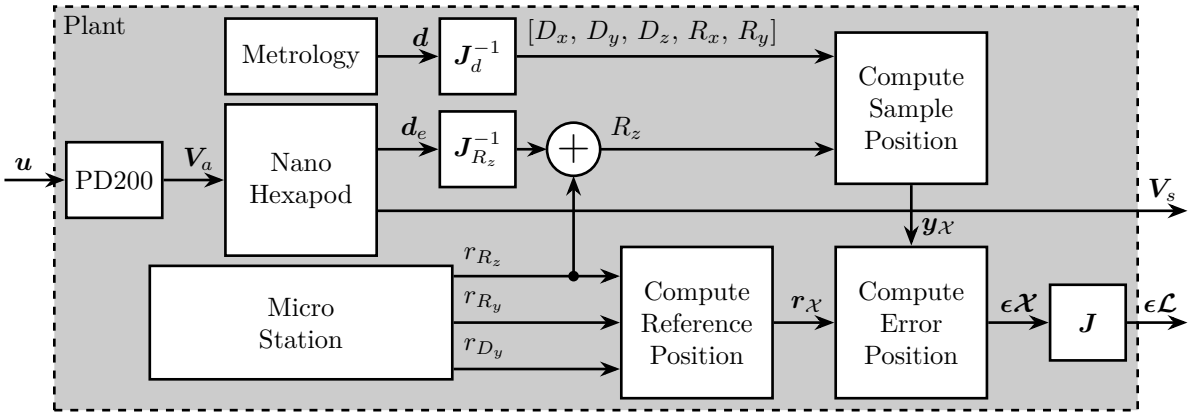

Figure 2.1: Schematic of the NASS plant

2.1 Open-Loop Plant Identification

The dynamics of the plant is first identified for a fixed spindle angle (at 0 deg) and without any payload. The model dynamics is also identified under the same conditions.

A comparison between the model and the measured dynamics is presented in Figure 2.2. A good match can be observed for the diagonal dynamics (except the high frequency modes which are not modeled).

However, the coupling of the transfer function from command signals $\boldsymbol{u}$ to the estimated strut motion from the external metrology $\boldsymbol{\epsilon\mathcal{L}}$ is larger than expected (Figure 2.2a).

The experimental time delay estimated from the FRF (Figure 2.2a) is larger than expected. After investigation, it was found that the additional delay was due to a digital processing unit[1] that was used to get the interferometers' signals in the Speedgoat. This issue was later solved.

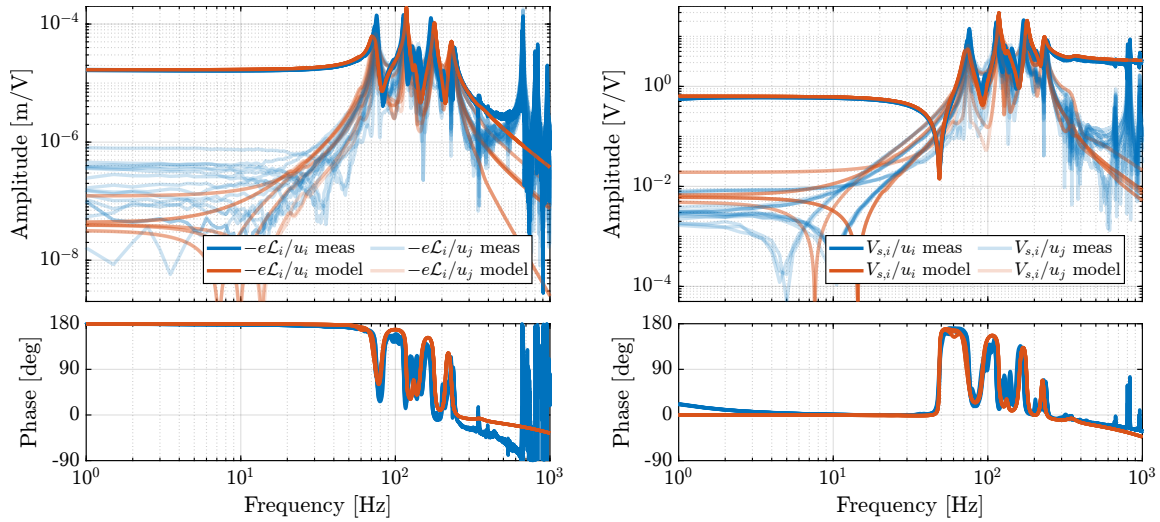

(a) External Metrology

(b) Force Sensors

Figure 2.2: Comparison between the measured dynamics and the multi-body model dynamics. Both for the external metrology (a) and force sensors (b). Direct terms are displayed with solid lines while off-diagonal (i.e. coupling) terms are displayed with shaded lines.

2.2 Better Angular Alignment

One possible explanation of the increased coupling observed in Figure 2.2a is the poor alignment between the external metrology axes (i.e. the interferometer supports) and the nano-hexapod axes. To estimate this alignment, a decentralized low-bandwidth feedback controller based on the nano-hexapod encoders was implemented. This allowed to perform two straight motions of the nano-hexapod along its x and y axes. During these two motions, external metrology measurements were recorded and the results are shown in Figure 2.3. It was found that there was a misalignment of 2.7 degrees (rotation along the vertical axis) between the interferometer axes and nano-hexapod axes. This was corrected by adding an offset to the spindle angle. After alignment, the same motion was performed using the nano-hexapod while recording the signal of the external metrology. Results shown in Figure 2.3b are indeed indicating much better alignment.

The dynamics of the plant was identified again after fine alignment and compared with the model dynamics in Figure 2.4. Compared to the initial identification shown in Figure 2.2a, the obtained coupling was decreased and was close to the coupling obtained with the multi-body model. At low frequency (below 10 Hz), all off-diagonal elements have an amplitude ≈ 100 times lower than the diagonal elements, indicating that a low bandwidth feedback controller can be implemented in a decentralized

[1] The "PEPU" [2] was used for digital protocol conversion between the interferometers and the Speedgoat.

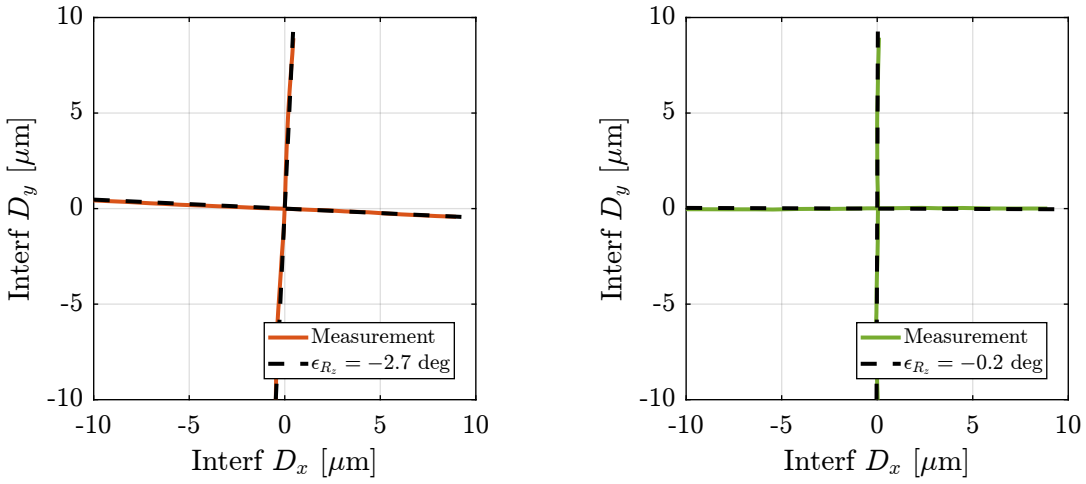

(a) Before alignment

(b) After alignment

Figure 2.3: Measurement of the Nano-Hexapod axes in the frame of the external metrology. Before alignment (a) and after alignment (b).

manner (i.e. 6 SISO controllers). Between 650 Hz and 1000 Hz, several modes can be observed, which are due to flexible modes of the top platform and the modes of the two spheres adjustment mechanism. The flexible modes of the top platform can be passively damped, whereas the modes of the two reference spheres should not be present in the final application.

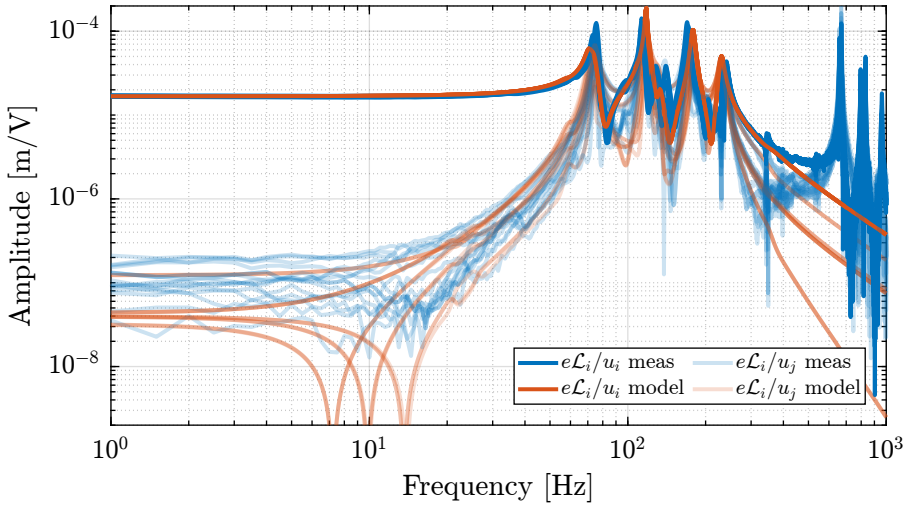

Figure 2.4: Decrease of the coupling with better Rz alignment

2.3 Effect of Payload Mass

To determine how the system dynamics changes with the payload, open-loop identification was performed for four payload conditions shown in Figure 2.5. The obtained direct terms are compared with the model dynamics in Figure 2.6. It was found that the model well predicts the measured dynamics

under all payload conditions. Therefore, the model can be used for model-based control if necessary.

It is interesting to note that the anti-resonances in the force sensor plant now appear as minimum-phase, as the model predicts (Figure 2.6b).

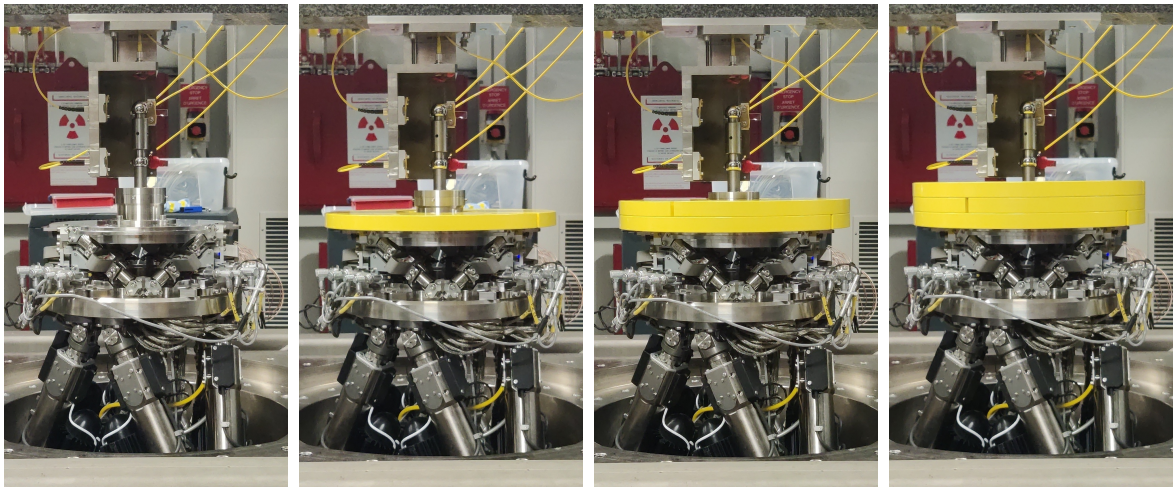

(a) $m = 0\,\text{kg}$ **(b)** $m = 13\,\text{kg}$ **(c)** $m = 26\,\text{kg}$ **(d)** $m = 39\,\text{kg}$

Figure 2.5: The four tested payload conditions. (a) without payload. (b) with 13 kg payload. (c) with 26 kg payload. (d) with 39 kg payload.

2.4 Effect of Spindle Rotation

To verify that all the kinematics in Figure 2.1 are correct and to check whether the system dynamics is affected by Spindle rotation of not, three identification experiments were performed: no spindle rotation, spindle rotation at $36\,\text{deg}/s$ and at $180\,\text{deg}/s$.

The obtained dynamics from command signal u to estimated strut error $\epsilon\mathcal{L}$ are displayed in Figure 2.7. Both direct terms (Figure 2.7a) and coupling terms (Figure 2.7b) are unaffected by the rotation. The same can be observed for the dynamics from command signal to encoders and to force sensors. This confirms that spindle's rotation has no significant effect on plant dynamics. This also indicates that the metrology kinematics is correct and is working in real time.

Conclusion

The identified frequency response functions from command signals $\boldsymbol{u}$ to the force sensors $\boldsymbol{V}_s$ and to the estimated strut errors $\boldsymbol{\epsilon\mathcal{L}}$ are well matching the dynamics of the developed multi-body model. The effect of payload mass is shown to be well predicted by the model, which can be useful if robust model based control is to be used. The spindle rotation had no visible effect on the measured dynamics, indicating that controllers should be robust against spindle rotation.

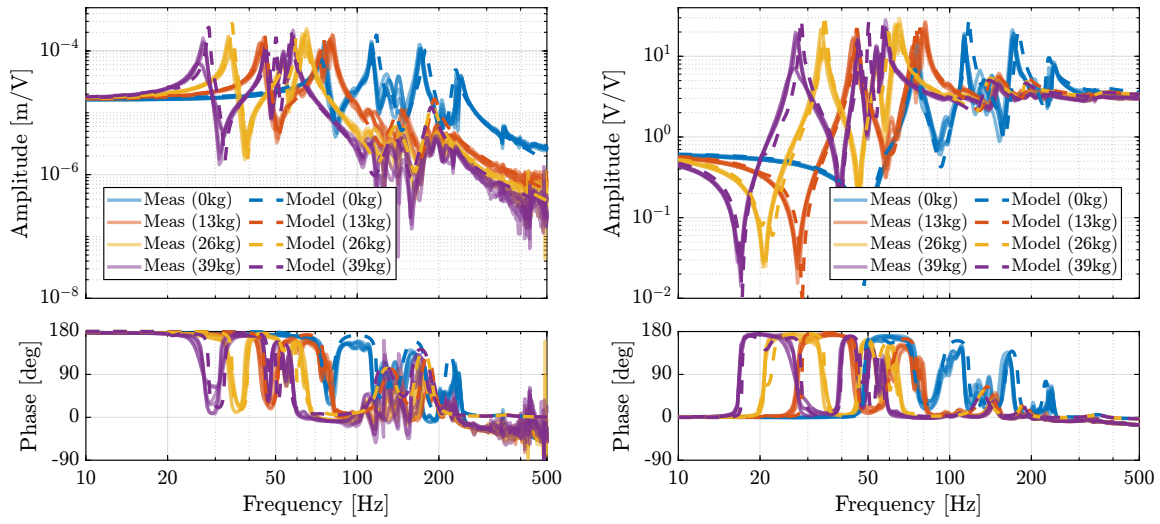

(a) from u to $\epsilon\mathcal{L}$ **(b)** from u to V_s

Figure 2.6: Comparison of the diagonal elements (i.e. "direct" terms) of the measured FRF matrix and the dynamics identified from the multi-body model. Both for the dynamics from u to $\epsilon\mathcal{L}$ (a) and from u to V_s (b)

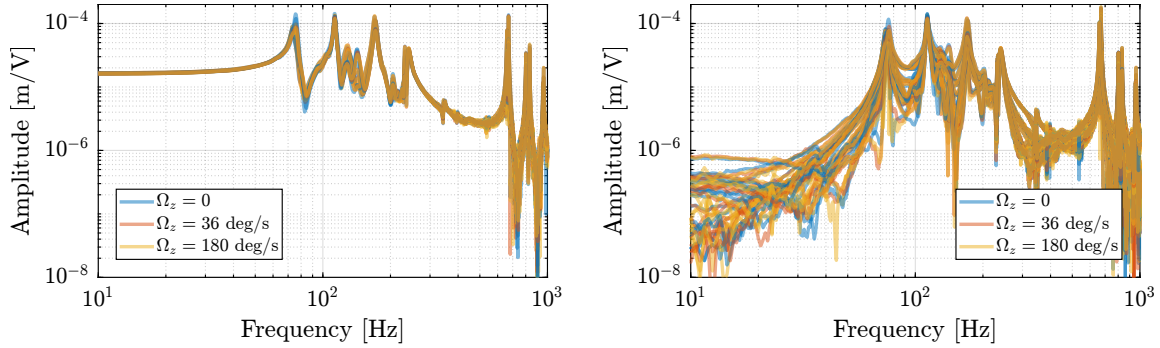

(a) Direct terms **(b)** Coupling terms

Figure 2.7: Effect of the spindle rotation on the plant dynamics from u to $\epsilon\mathcal{L}$. Three rotational velocities are tested ($0\,\text{deg}/s$, $36\,\text{deg}/s$ and $180\,\text{deg}/s$). Both direct terms (a) and coupling terms (b) are displayed.

3 Decentralized Integral Force Feedback

In this section, the low authority control part is first validated. It consists of a decentralized Integral Force Feedback controller $\boldsymbol{K}_{\text{IFF}}$, with all the diagonal terms being equal (3.2).

$$\boldsymbol{K}_{\text{IFF}} = K_{\text{IFF}} \cdot \boldsymbol{I}_6 = \begin{bmatrix} K_{\text{IFF}} & & 0 \\ & \ddots & \\ 0 & & K_{\text{IFF}} \end{bmatrix} \tag{3.1}$$

The decentralized Integral Force Feedback is implemented as shown in the block diagram of Figure 3.1.

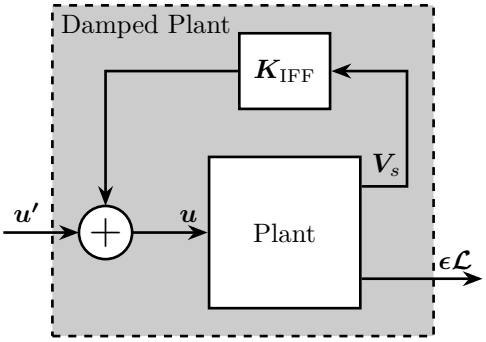

Figure 3.1: Block diagram of the implemented decentralized IFF controller. The controller $\boldsymbol{K}_{\text{IFF}}$ is a diagonal controller with the same elements for every diagonal term K_{IFF}.

3.1 IFF Plant

As the multi-body model is used to evaluate the stability of the IFF controller and to optimize the achievable damping, it is first checked whether this model accurately represents the system dynamics.

In the previous section (Figure 2.6b), it was shown that the model well captures the dynamics from each actuator to its collocated force sensor, and that for all considered payloads. Nevertheless, it is also important to model accurately the coupling in the system. To verify that, instead of comparing the 36 elements of the 6×6 frequency response matrix from $\boldsymbol{u}$ to $\boldsymbol{V_s}$, only 6 elements are compared in Figure 3.2. Similar results were obtained for all other 30 elements and for the different payload conditions. This confirms that the multi-body model can be used to tune the IFF controller.

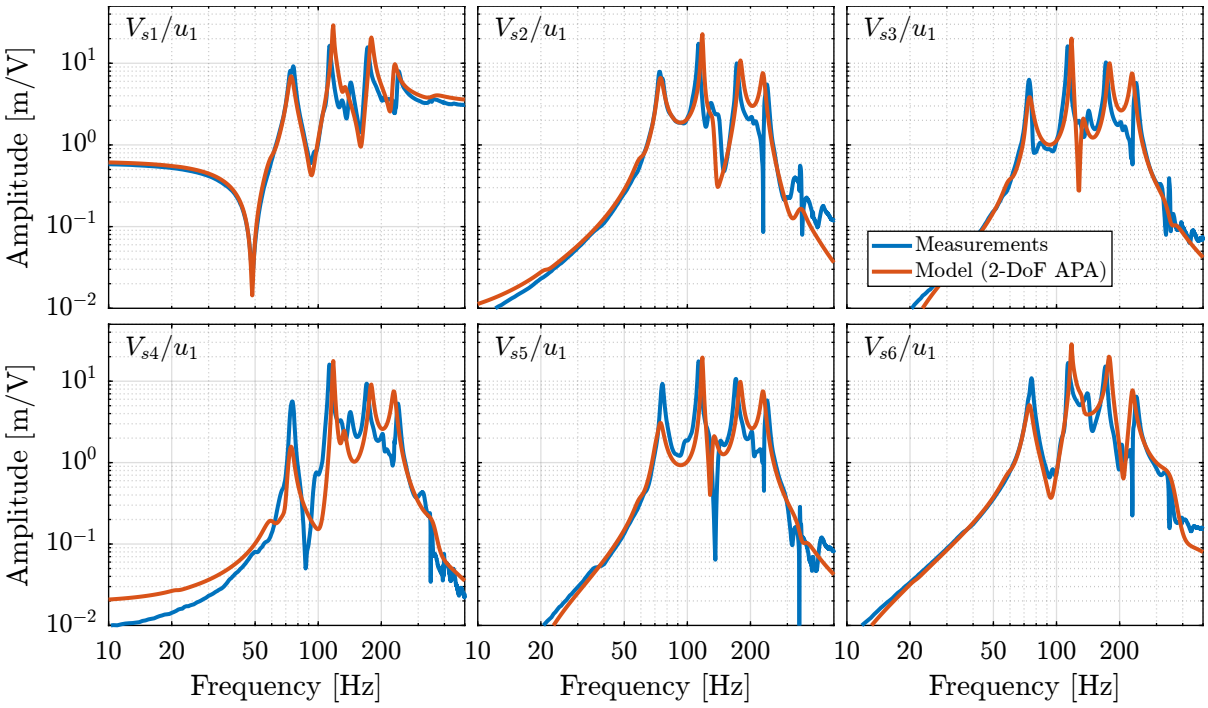

Figure 3.2: Comparison of the measured (in blue) and modeled (in red) frequency transfer functions from the first control signal u_1 to the six force sensor voltages V_{s1} to V_{s6}

3.2 IFF Controller

A decentralized IFF controller was designed to add damping to the suspension modes of the nano-hexapod for all considered payloads. The frequency of the suspension modes are ranging from $\approx 30\,\text{Hz}$ to $\approx 250\,\text{Hz}$ (Figure 2.6b), and therefore, the IFF controller should provide integral action in this frequency range. A second-order high-pass filter (cut-off frequency of $10\,\text{Hz}$) was added to limit the low frequency gain (3.2).

$$K_{\text{IFF}} = g_0 \cdot \underbrace{\frac{1}{s}}_{\text{int}} \cdot \underbrace{\frac{s^2/\omega_z^2}{s^2/\omega_z^2 + 2\xi_z s/\omega_z + 1}}_{\text{2nd order LPF}}, \quad (g_0 = -100,\ \omega_z = 2\pi 10\,\text{rad/s},\ \xi_z = 0.7) \tag{3.2}$$

The bode plot of the decentralized IFF controller is shown in Figure 3.3a and the "decentralized loop-gains" for all considered payload masses are shown in Figure 3.3b. It can be seen that the loop-gain is larger than 1 around the suspension modes, which indicates that some damping should be added to the suspension modes.

To estimate the added damping, a root-locus plot was computed using the multi-body model (Figure 3.4). It can be seen that for all considered payloads, the poles are bounded to the "left-half plane" indicating that the decentralized IFF is robust. The closed-loop poles for the chosen gain value are represented by black crosses. It can be seen that while damping can be added for all payloads (as compared to the open-loop case), the optimal value of the gain is different for each payload. For low payload masses, a higher IFF controller gain can lead to better damping. However, in this study, it was chosen to implement a "fixed" (i.e. non-adaptive) decentralized IFF controller.

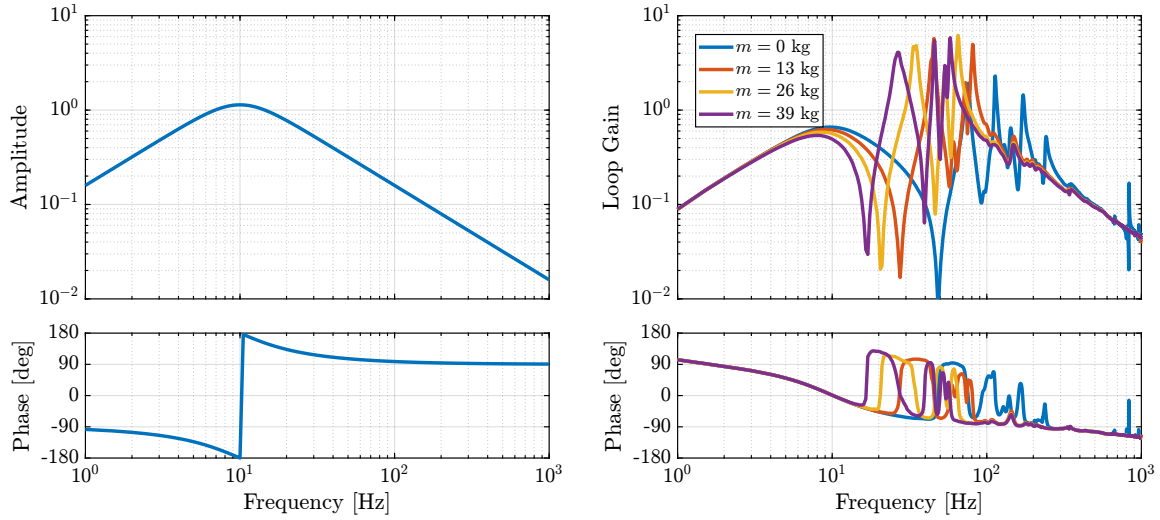

(a) Bode plot of K_{IFF}

(b) Decentralized Loop gains

Figure 3.3: Bode plot of the decentralized IFF controller (a). The decentralized controller K_{IFF} multiplied by the identified dynamics from u_1 to V_{s1} for all payloads are shown in (b)

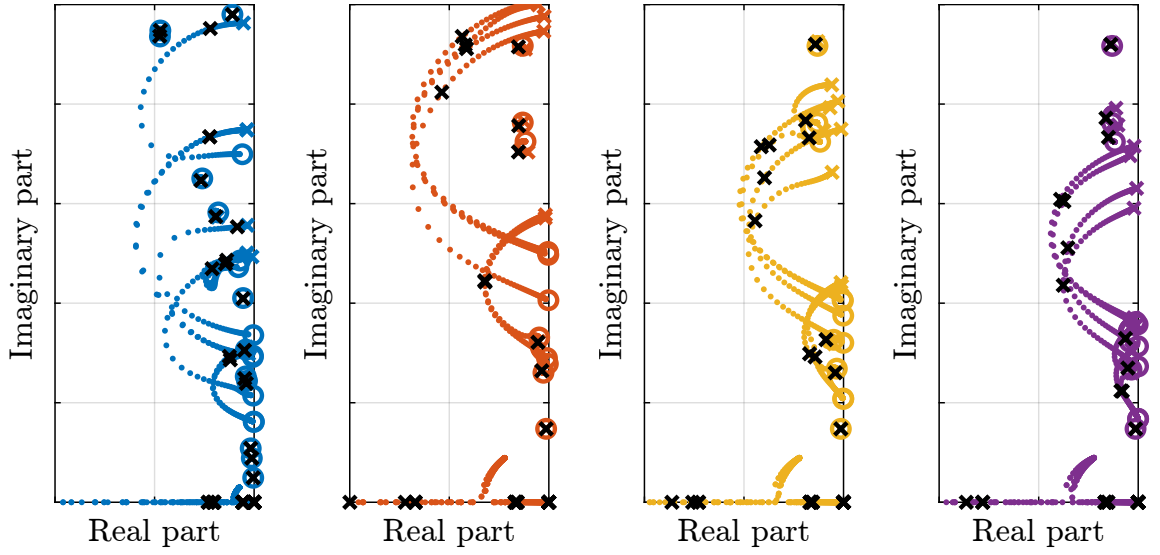

(a) $m = 0\,\text{kg}$ **(b)** $m = 13\,\text{kg}$ **(c)** $m = 26\,\text{kg}$ **(d)** $m = 39\,\text{kg}$

Figure 3.4: Root Locus plots for the designed decentralized IFF controller, computed using the multy-body model. Black crosses indicate the closed-loop poles for the choosen value of the gain.

3.3 Damped Plant

As the model accurately represents the system dynamics, it can be used to estimate the damped plant, i.e. the transfer functions from $\boldsymbol{u}'$ to $\boldsymbol{\mathcal{L}}$. The obtained damped plants are compared to the open-loop plants in Figure 3.5a. The peak amplitudes corresponding to the suspension modes were approximately reduced by a factor 10 for all considered payloads, indicating the effectiveness of the decentralized IFF control strategy.

To experimentally validate the Decentralized IFF controller, it was implemented and the damped plants (i.e. the transfer function from $\boldsymbol{u}'$ to $\boldsymbol{\epsilon\mathcal{L}}$) were identified for all payload conditions. The obtained frequency response functions are compared with the model in Figure 3.5b verifying the good correlation between the predicted damped plant using the multi-body model and the experimental results.

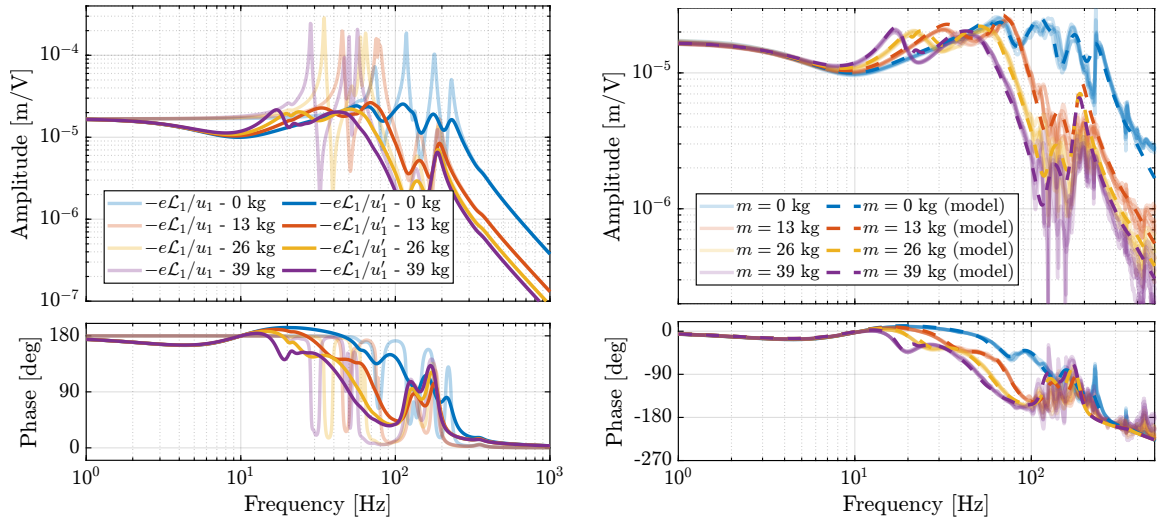

(a) Effect of IFF on the plant

(b) Comparison of model and experimental results

Figure 3.5: Comparison of the open-loop plants and the damped plant with Decentralized IFF, estimated from the multi-body model (a). Comparison of measured damped and modeled plants for all considered payloads (b). Only "direct" terms ($\epsilon\mathcal{L}_i/u_i'$) are displayed for simplificty

Conclusion

The implementation of a decentralized Integral Force Feedback controller was successfully demonstrated. Using the multi-body model, the controller was designed and optimized to ensure stability across all payload conditions while providing significant damping of suspension modes. The experimental results validated the model predictions, showing a reduction in peak amplitudes by approximately a factor of 10 across the full payload range (0-39 kg). Although higher gains could achieve better damping performance for lighter payloads, the chosen fixed-gain configuration represents a robust compromise that maintains stability and performance under all operating conditions. The good correlation between the modeled and measured damped plants confirms the effectiveness of using the multi-body model for both controller design and performance prediction.

4 High Authority Control in the frame of the struts

In this section, a High-Authority-Controller is developed to actively stabilize the sample position. The corresponding control architecture is shown in Figure 4.1.

As the diagonal terms of the damped plants were found to be all equal (thanks to the system's symmetry and manufacturing and mounting uniformity, see Figure 3.5b), a diagonal high authority controller $\boldsymbol{K}_{\text{HAC}}$ is implemented with all diagonal terms being equal (4.1).

$$\boldsymbol{K}_{\text{HAC}} = K_{\text{HAC}} \cdot \boldsymbol{I}_6 = \begin{bmatrix} K_{\text{HAC}} & & 0 \\ & \ddots & \\ 0 & & K_{\text{HAC}} \end{bmatrix} \tag{4.1}$$

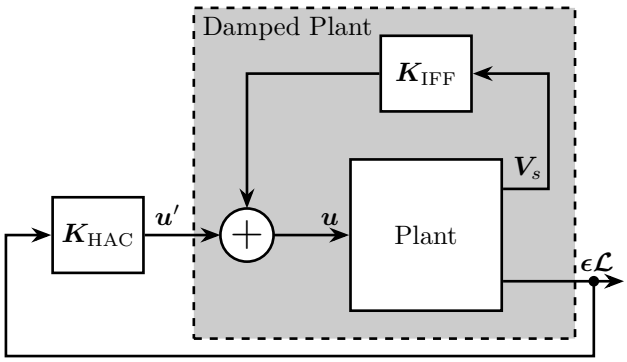

Figure 4.1: Block diagram of the implemented HAC-IFF controllers. The controller $\boldsymbol{K}_{\text{HAC}}$ is a diagonal controller with the same elements on every diagonal term K_{HAC}.

4.1 Damped Plant

To verify whether the multi-body model accurately represents the measured damped dynamics, both the direct terms and coupling terms corresponding to the first actuator are compared in Figure 4.2. Considering the complexity of the system's dynamics, the model can be considered to represent the system's dynamics with good accuracy, and can therefore be used to tune the feedback controller and evaluate its performance.

The challenge here is to tune a high authority controller such that it is robust to the change in dynamics due to different payloads being used. Without using the HAC-LAC strategy, it would be necessary to design a controller that provides good performance for all undamped dynamics (blue curves in Figure 4.3), which is a very complex control problem. With the HAC-LAC strategy, the designed controller

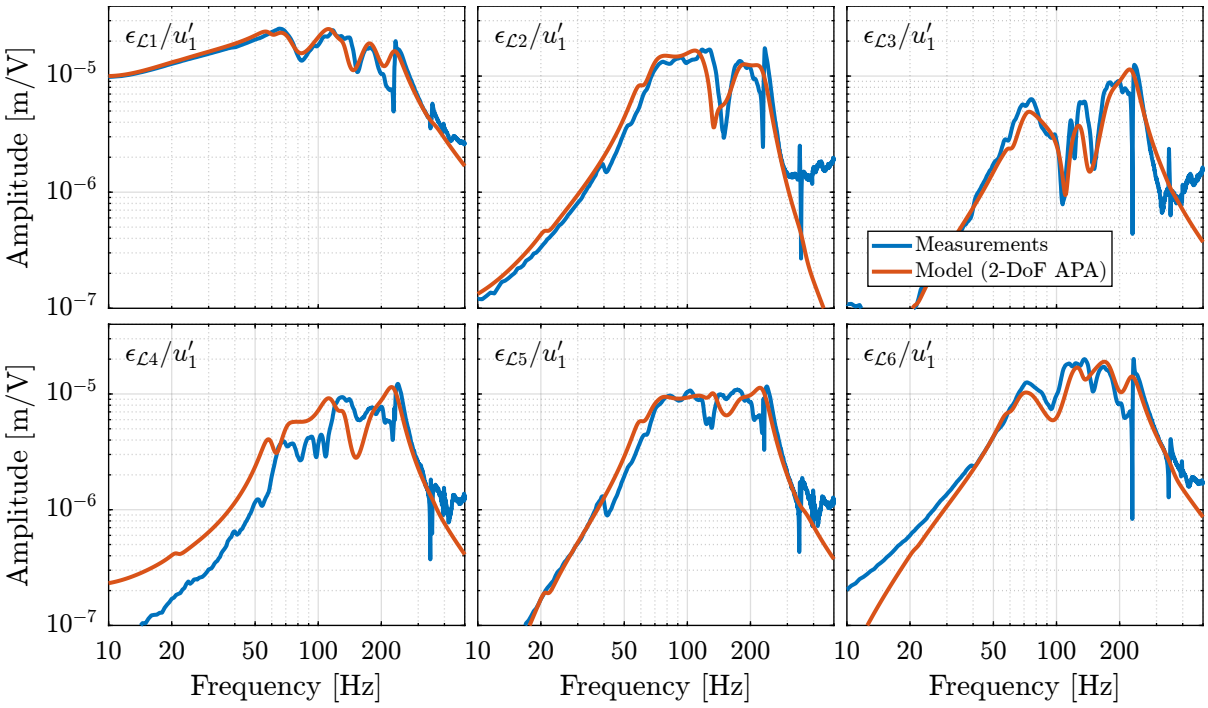

Figure 4.2: Comparison of the measured (in blue) and modeled (in red) frequency transfer functions from the first control signal (u'_1) of the damped plant to the estimated errors ($\epsilon_{\mathcal{L}_i}$) in the frame of the six struts by the external metrology

must be robust to all the damped dynamics (red curves in Figure 4.3), which is easier from a control perspective. This is one of the key benefits of using the HAC-LAC strategy.

4.2 Interaction Analysis

The control strategy here is to apply a diagonal control in the frame of the struts; thus, it is important to determine the frequency at which the multivariable effects become significant, as this represents a critical limitation of the control approach. To conduct this interaction analysis, the Relative Gain Array (RGA) $\boldsymbol{\Lambda_G}$ is first computed using (4.2) for the plant dynamics identified with the multiple payload masses.

$$\boldsymbol{\Lambda_G}(\omega) = \boldsymbol{G}(j\omega) \star \left(\boldsymbol{G}(j\omega)^{-1}\right)^T, \quad (\star \text{ means element wise multiplication}) \tag{4.2}$$

Then, RGA numbers are computed using (4.3) and are use as a metric for interaction [3, chapt. 3.4].

$$\text{RGA number}(\omega) = \|\boldsymbol{\Lambda_G}(\omega) - \boldsymbol{I}\|_{\text{sum}} \tag{4.3}$$

The obtained RGA numbers are compared in Figure 4.4. The results indicate that higher payload masses increase the coupling when implementing control in the strut reference frame (i.e., decentralized approach). This indicates that achieving high bandwidth feedback control is increasingly challenging as

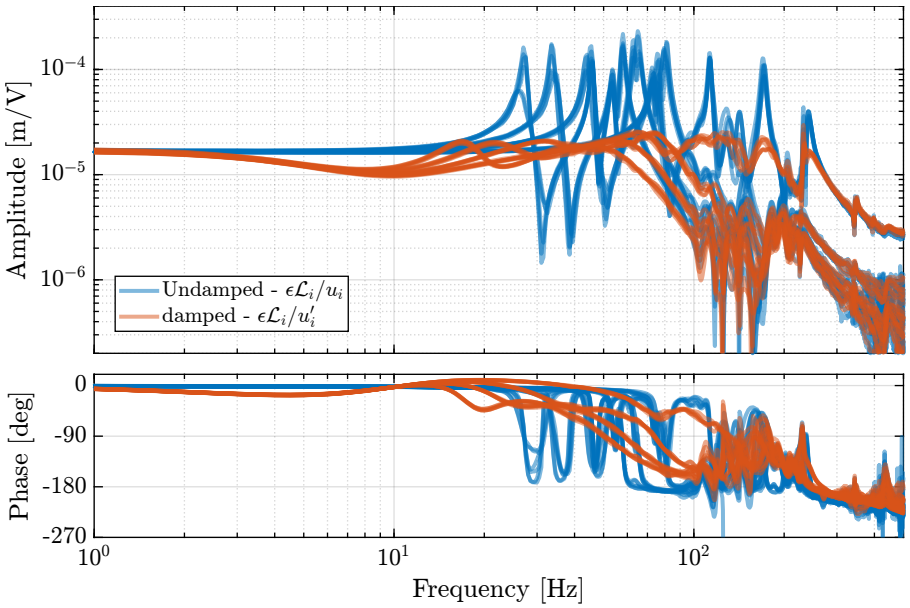

Figure 4.3: Comparison of the (six) direct terms for all (four) payload conditions in the undamped case (in blue) and the damped case (i.e. with the decentralized IFF being implemented, in red).

the payload mass increases. This behavior can be attributed to the fundamental approach of implementing control in the frame of the struts. Above the suspension modes of the nano-hexapod, the motion induced by the piezoelectric actuators is no longer dictated by kinematics but rather by the inertia of the different parts. This design choice, while beneficial for system simplicity, introduces inherent limitations in the system's ability to handle larger masses at high frequency.

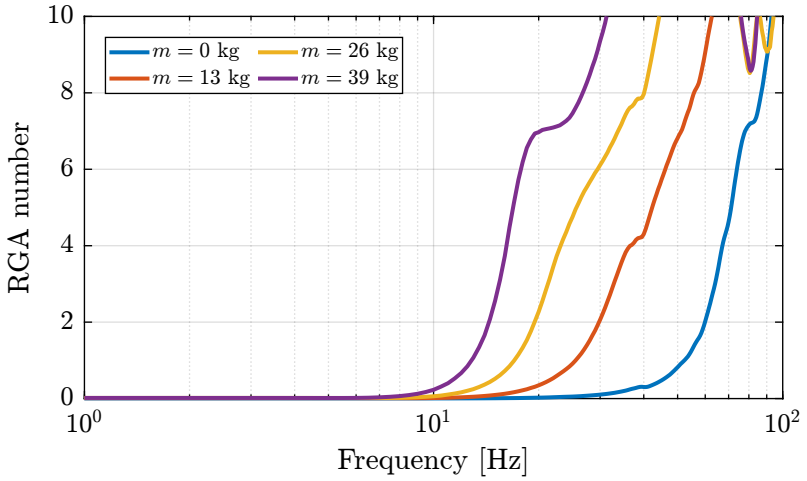

Figure 4.4: RGA-number for the damped plants - Comparison of all the payload conditions

4.3 Robust Controller Design

A diagonal controller was designed to be robust against changes in payload mass, which means that every damped plant shown in Figure 4.3 must be considered during the controller design. For this controller design, a crossover frequency of 5 Hz was chosen to limit the multivariable effects, as explain in Section 4.2. One integrator is added to increase the low-frequency gain, a lead is added around 5 Hz to increase the stability margins and a first-order low-pass filter with a cut-off frequency of 30 Hz is added to improve the robustness to dynamical uncertainty at high frequency. The controller transfer function is shown in (4.4).

$$K_{\text{HAC}}(s) = g_0 \cdot \underbrace{\frac{\omega_c}{s}}_{\text{int}} \cdot \underbrace{\frac{1}{\sqrt{\alpha}} \frac{1 + \frac{s}{\omega_c/\sqrt{\alpha}}}{1 + \frac{s}{\omega_c\sqrt{\alpha}}}}_{\text{lead}} \cdot \underbrace{\frac{1}{1 + \frac{s}{\omega_0}}}_{\text{LPF}}, \quad (\omega_c = 2\pi 5\,\text{rad/s},\ \alpha = 2,\ \omega_0 = 2\pi 30\,\text{rad/s}) \tag{4.4}$$

The obtained "decentralized" loop-gains (i.e. the diagonal element of the controller times the diagonal terms of the plant) are shown in Figure 4.5a. The closed-loop stability was verified by computing the characteristic Loci (Figure 4.5b). However, small stability margins were observed for the highest mass, indicating that some multivariable effects are in play.

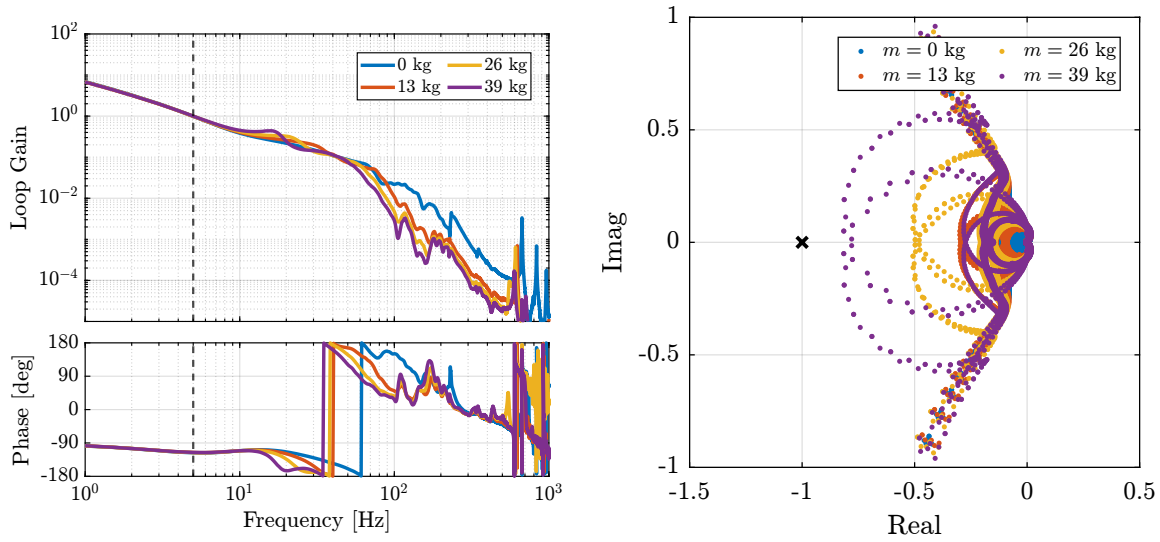

(a) Loop Gains

(b) Characteristic Loci

Figure 4.5: Robust High Authority Controller. "Decentralized loop-gains" are shown in (a) and characteristic loci are shown in (b)

4.4 Performance estimation with simulation of Tomography scans

To estimate the performances that can be expected with this HAC-LAC architecture and the designed controller, simulations of tomography experiments were performed[1]. The rotational velocity was set to 180 deg/s, and no payload was added on top of the nano-hexapod. An open-loop simulation and a closed-loop simulation were performed and compared in Figure 4.6. The obtained closed-loop positioning accuracy was found to comply with the requirements as it succeeded to keep the point of interest on the beam (Figure 4.6b).

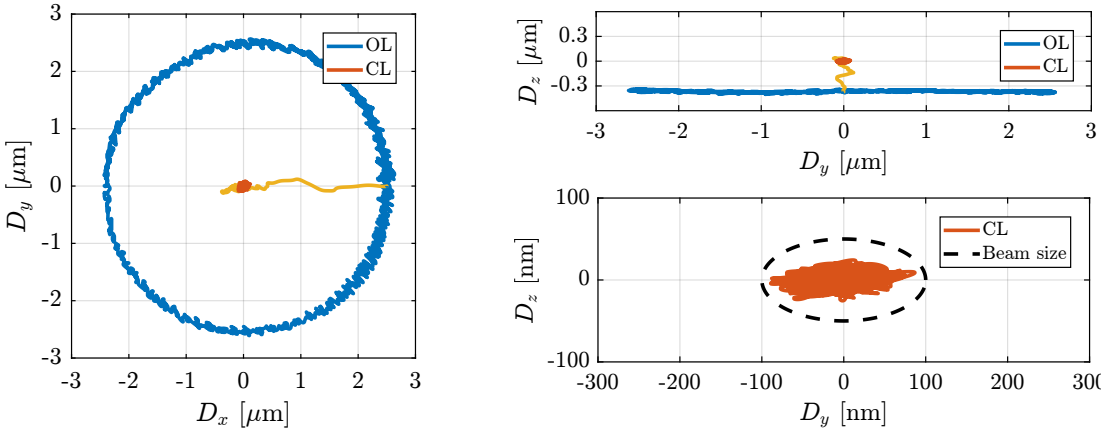

(a) XY plane

(b) YZ plane

Figure 4.6: Position error of the sample in the XY (a) and YZ (b) planes during a simulation of a tomography experiment at 180 deg/s. No payload is placed on top of the nano-hexapod.

4.5 Robustness estimation with simulation of Tomography scans

To verify the robustness against payload mass variations, four simulations of tomography experiments were performed with payloads as shown Figure 2.5 (i.e. 0 kg, 13 kg, 26 kg and 39 kg). The rotational velocity was set at 6 deg/s, which is the typical rotational velocity for heavy samples.

The closed-loop systems were stable under all payload conditions, indicating good control robustness. However, the positioning errors worsen as the payload mass increases, especially in the lateral D_y direction, as shown in Figure 4.7. However, it was decided that this controller should be tested experimentally and improved only if necessary.

Conclusion

In this section, a High-Authority-Controller was developed to actively stabilize the sample position. The multi-body model was first validated by comparing it with the measured frequency responses of the damped plant, which showed good agreement for both direct terms and coupling terms. This

[1] Note that the eccentricity of the "point of interest" with respect to the Spindle rotation axis has been tuned based on measurements.

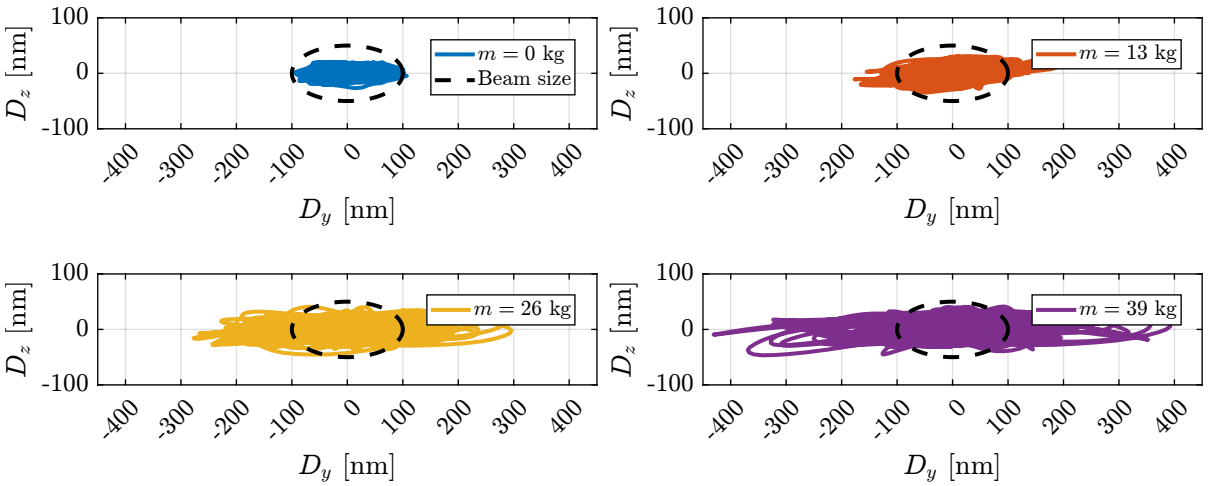

Figure 4.7: Positioning errors in the Y-Z plane during tomography experiments simulated using the multi-body model (in closed-loop)

validation confirmed that the model can be reliably used to tune the feedback controller and evaluate its performance.

An interaction analysis using the RGA-number was then performed, which revealed that higher payload masses lead to increased coupling when implementing control in the strut reference frame. Based on this analysis, a diagonal controller with a crossover frequency of 5 Hz was designed, incorporating an integrator, a lead compensator, and a first-order low-pass filter.

Finally, tomography experiments were simulated to validate the HAC-LAC architecture. The closed-loop system remained stable under all tested payload conditions (0 to 39 kg). With no payload at 180 deg/s, the NASS successfully maintained the sample point of interest in the beam, which fulfilled the specifications. At 6 deg/s, although the positioning errors increased with the payload mass (particularly in the lateral direction), the system remained stable. These results demonstrate both the effectiveness and limitations of implementing control in the frame of the struts.

5 Validation with Scientific experiments

In this section, the goal is to evaluate the performance of the NASS and validate its use to perform typical scientific experiments. However, the online metrology prototype (presented in Section 1) does not allow samples to be placed on top of the nano-hexapod while being illuminated by the x-ray beam. Nevertheless, to fully validate the NASS, typical motions performed during scientific experiments can be mimicked, and the positioning performances can be evaluated.

Several scientific experiments were replicated, such as:

- Tomography scans: continuous rotation of the Spindle along the vertical axis (Section 5.1)
- Reflectivity scans: R_y rotations using the tilt-stage (Section 5.2)
- Vertical layer scans: D_z step motion or ramp scans using the nano-hexapod (Section 5.3)
- Lateral scans: D_y scans using the T_y translation stage (Section 5.4)
- Diffraction Tomography:continuous R_z rotation using the Spindle and lateral D_y scans performed at the same time using the translation stage (Section 5.5)

Unless explicitly stated, all closed-loop experiments were performed using the robust (i.e. conservative) high authority controller designed in Section 4.3.

For each experiment, the obtained performances are compared to the specifications for the most demanding case in which nano-focusing optics are used to focus the beam down to $200\,nm \times 100\,nm$. In this case, the goal is to keep the sample's point of interest in the beam, and therefore the D_y and D_z positioning errors should be less than $200\,nm$ and $100\,nm$ peak-to-peak, respectively. The R_y error should be less than $1.7\,\mu$rad peak-to-peak. In terms of RMS errors, this corresponds to $30\,nm$ in D_y, $15\,nm$ in D_z and 250 nrad in R_y (a summary of the specifications is given in Table 5.1).

Results obtained for all experiments are summarized and compared to the specifications in Section 5.5.

Table 5.1: Specifications for the Nano-Active-Stabilization-System

	D_y	D_z	R_y
peak 2 peak	200nm	100nm	$1.7\,\mu$rad
RMS	30nm	15nm	250 nrad

5.1 Tomography Scans

Slow Tomography scans First, tomography scans were performed with a rotational velocity of 6 deg/s for all considered payload masses (shown in Figure 2.5). Each experimental sequence consisted of two complete spindle rotations: an initial open-loop rotation followed by a closed-loop rotation. The experimental results for the 26 kg payload are presented in Figure 5.1a.

Due to the static deformation of the micro-station stages under payload loading, a significant eccentricity was observed between the point of interest and the spindle rotation axis. To establish a theoretical lower bound for open-loop errors, an ideal scenario was assumed, where the point of interest perfectly aligns with the spindle rotation axis. This idealized case was simulated by first calculating the eccentricity through circular fitting (represented by the dashed black circle in Figure 5.1a), and then subtracting it from the measured data, as shown in Figure 5.1b. While this approach likely underestimates actual open-loop errors, as perfect alignment is practically unattainable, it enables a more balanced comparison with closed-loop performance.

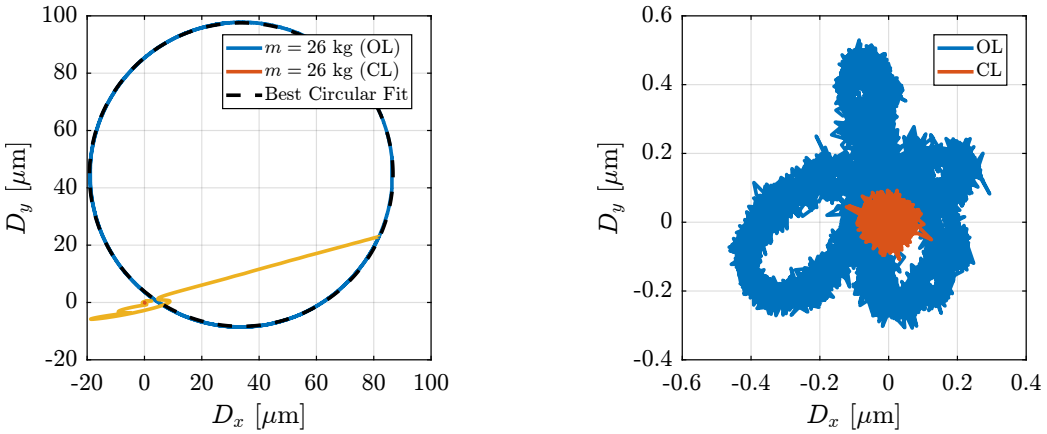

(a) Errors in (x, y) plane

(b) Removed eccentricity

Figure 5.1: Tomography experiment with a rotation velocity of 6 deg/s, and payload mass of 26kg. Errors in the (x, y) plane are shown in (a). The estimated eccentricity is represented by the black dashed circle. The errors with subtracted eccentricity are shown in (b).

The residual motion (i.e. after compensating for eccentricity) in the $Y - Z$ is compared against the minimum beam size, as illustrated in Figure 5.2. Results are indicating the NASS succeeds in keeping the sample's point of interest on the beam, except for the highest mass of 39 kg for which the lateral motion is a bit too high. These experimental findings are consistent with the predictions from the tomography simulations presented in Section 4.5.

Fast Tomography scans A tomography experiment was then performed with the highest rotational velocity of the Spindle: 180 deg/s[1]. The trajectory of the point of interest during the fast tomography scan is shown in Figure 5.3. Although the experimental results closely match the simulation results (Figure 4.6), the actual performance was slightly lower than predicted. Nevertheless, even with this robust (i.e. conservative) HAC implementation, the system performance was already close to the specified requirements.

[1]The highest rotational velocity of 360 deg/s could not be tested due to an issue in the Spindle's controller.

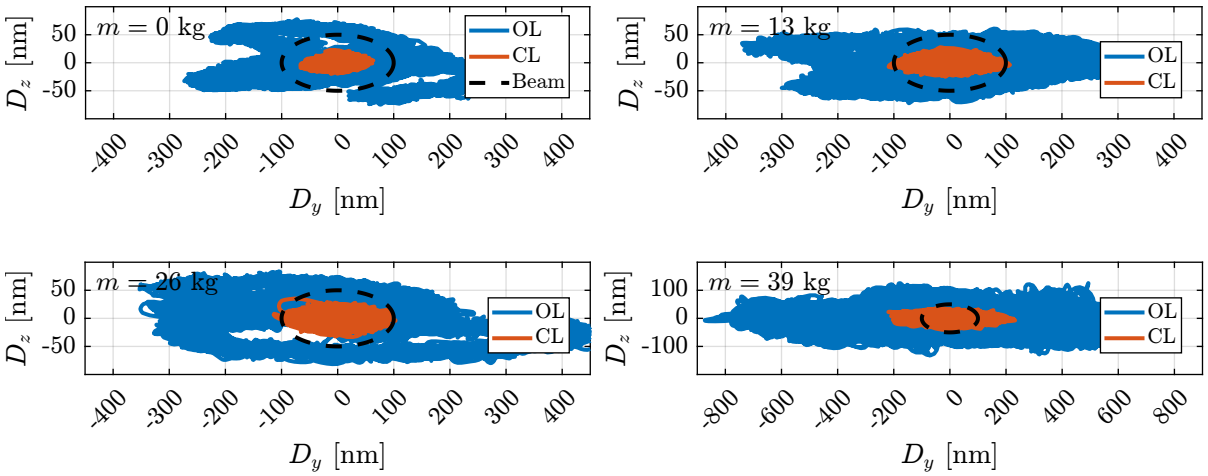

Figure 5.2: Measured errors in the $Y - Z$ plane during tomography experiments at 6 deg/s for all considered payloads. In the open-loop case, the effect of eccentricity is removed from the data.

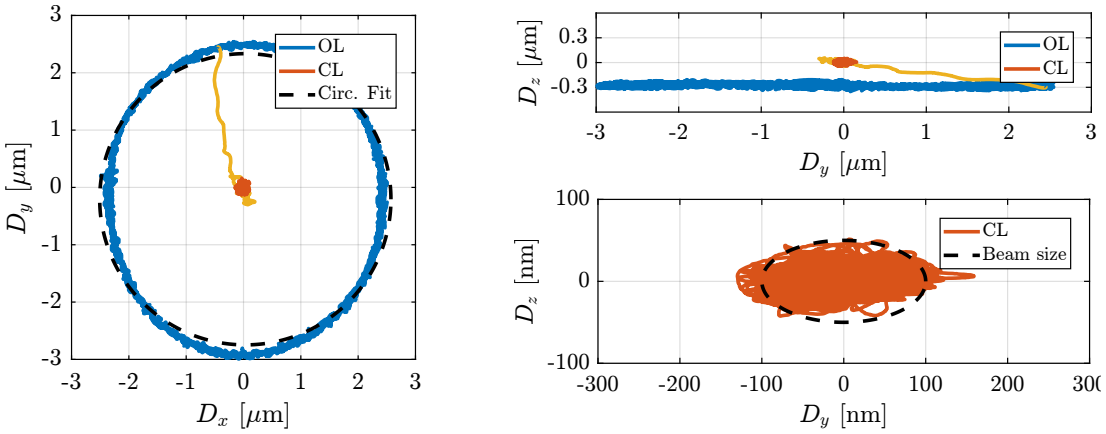

(a) XY plane

(b) YZ plane

Figure 5.3: Experimental results of tomography experiment at 180 deg/s without payload. The position error of the sample is shown in the XY (a) and YZ (b) planes.

Cumulative Amplitude Spectra A comparative analysis was conducted using three tomography scans at 180 deg/s to evaluate the effectiveness of the HAC-LAC strategy in reducing positioning errors. The scans were performed under three conditions: open-loop, with decentralized IFF control, and with the complete HAC-LAC strategy. For these specific measurements, an enhanced high authority controller was optimized for low payload masses to meet the performance requirements.

Figure 5.4 presents the cumulative amplitude spectra of the position errors for all three cases. The results reveal two distinct control contributions: the decentralized IFF effectively attenuates vibrations near the nano-hexapod suspension modes (an achievement not possible with HAC alone), while the high authority controller suppresses low-frequency vibrations primarily arising from Spindle guiding errors. Notably, the spectral patterns in Figure 5.4 closely resemble the cumulative amplitude spectra computed in the project's early stages.

This experiment also illustrates that when needed, performance can be enhanced by designing controllers for specific experimental conditions rather than relying solely on robust controllers that can accommodate all payload ranges.

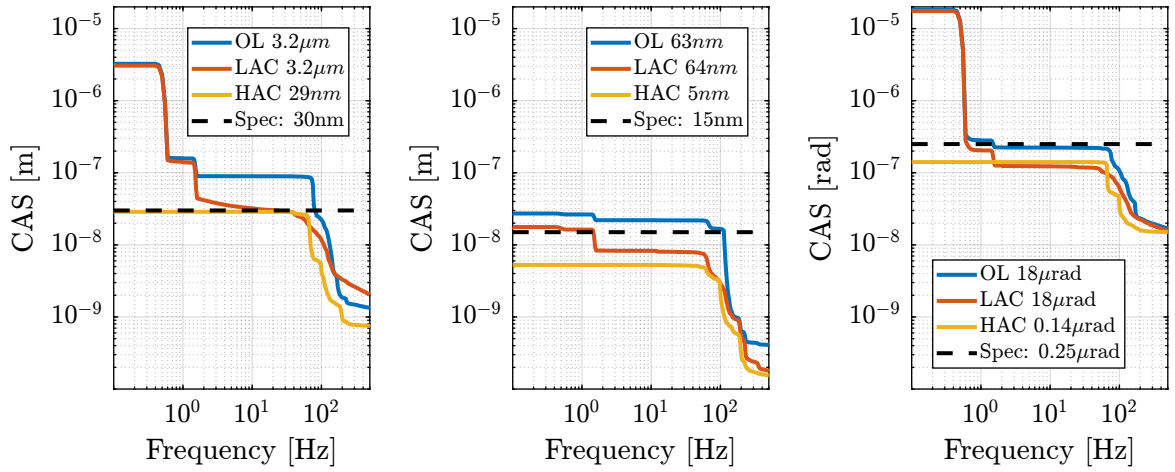

(a) D_y **(b)** D_z **(c)** R_y

Figure 5.4: Cumulative Amplitude Spectrum for tomography experiments at 180 deg/s. Open-Loop case, IFF, and HAC-LAC are compared. Specifications are indicated by black dashed lines. The RMS values are indicated in the legend.

5.2 Reflectivity Scans

X-ray reflectivity measurements involve scanning thin structures, particularly solid/liquid interfaces, through the beam by varying the R_y angle. In this experiment, a R_y scan was executed at a rotational velocity of 100 $\mu rad/s$, and the closed-loop positioning errors were monitored (Figure 5.5). The results confirmed that the NASS successfully maintained the point of interest within the specified beam parameters throughout the scanning process.

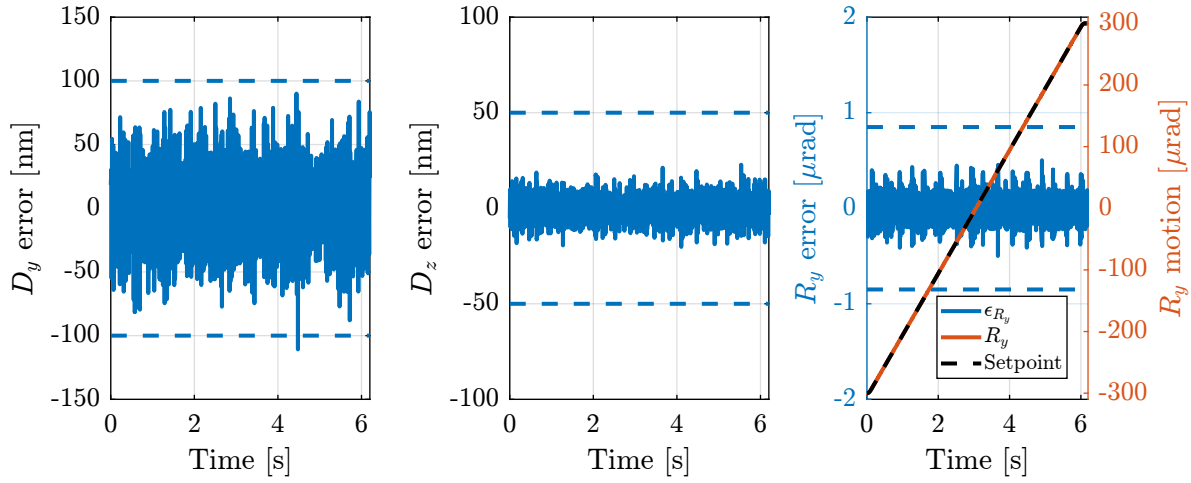

(a) D_y **(b)** D_z **(c)** R_y

Figure 5.5: Reflectivity scan (R_y) with a rotational velocity of 100 μrad/s.

5.3 Dirty Layer Scans

In some cases, samples are composed of several atomic "layers" that are first aligned in the horizontal plane through R_x and R_y positioning, followed by vertical scanning with precise D_z motion. These vertical scans can be executed either continuously or in a step-by-step manner.

Step by Step D_z motion The vertical step motion was performed exclusively with the nano-hexapod. Testing was conducted across step sizes ranging from 10 nm to 1 μm. Results are presented in Figure 5.6. The system successfully resolved 10nm steps (red curve in Figure 5.6a) if a 50ms integration time is considered for the detectors, which is compatible with many experimental requirements.

In step-by-step scanning procedures, the settling time is a critical parameter as it significantly affects the total experiment duration. The system achieved a response time of approximately 70 ms to reach the target position (within $\pm$20 nm), as demonstrated by the 1 μm step response in Figure 5.6c. The settling duration typically decreases for smaller step sizes.

Continuous D_z motion: Dirty Layer Scans For these and subsequent experiments, the NASS performs "ramp scans" (constant velocity scans). To eliminate tracking errors, the feedback controller incorporates two integrators, compensating for the plant's lack of integral action at low frequencies.

Initial testing at 10 $\mu m/s$ demonstrated positioning errors well within specifications (indicated by dashed lines in Figure 5.7).

A subsequent scan at 100 $\mu m/s$ - the maximum velocity for high-precision D_z scans[2] - maintains positioning errors within specifications during the constant velocity phase, with deviations occurring only during acceleration and deceleration phases (Figure 5.8). Since detectors typically operate only during the constant velocity phase, these transient deviations do not compromise the measurement quality.

[2]Such scan could corresponding to a 1ms integration time (which is typically the smallest integration time) and 100nm "resolution" (equal to the vertical beam size).

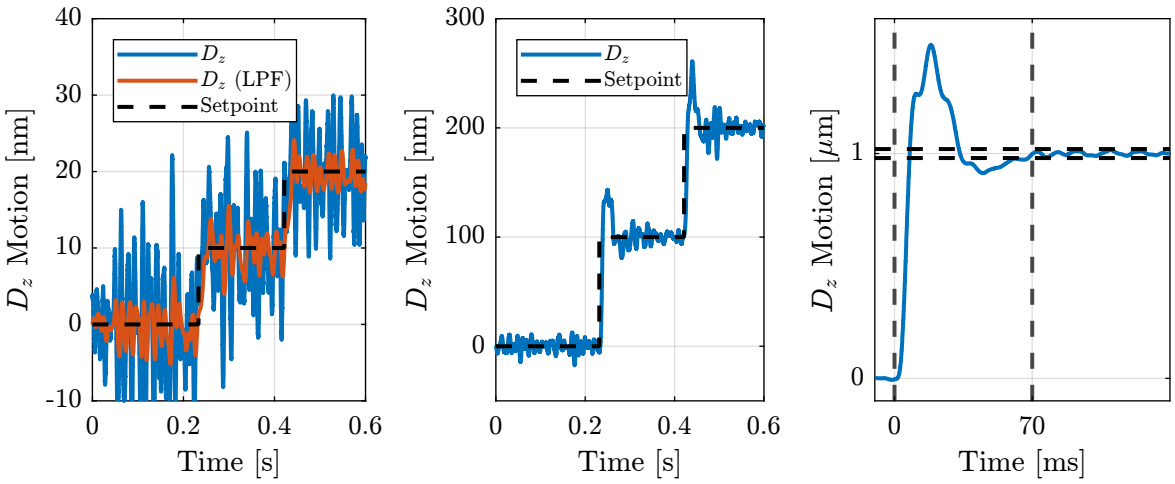

(a) 10nm steps **(b)** 100nm steps **(c)** 1 μm step

Figure 5.6: Vertical steps performed with the nano-hexapod. 10nm steps are shown in (a) with the low-pass filtered data corresponding to an integration time of 50 ms. 100nm steps are shown in (b). The response time to reach a peak-to-peak error of $\pm 20\,nm$ is $\approx 70\,ms$ as shown in (c) for a 1 μm step.

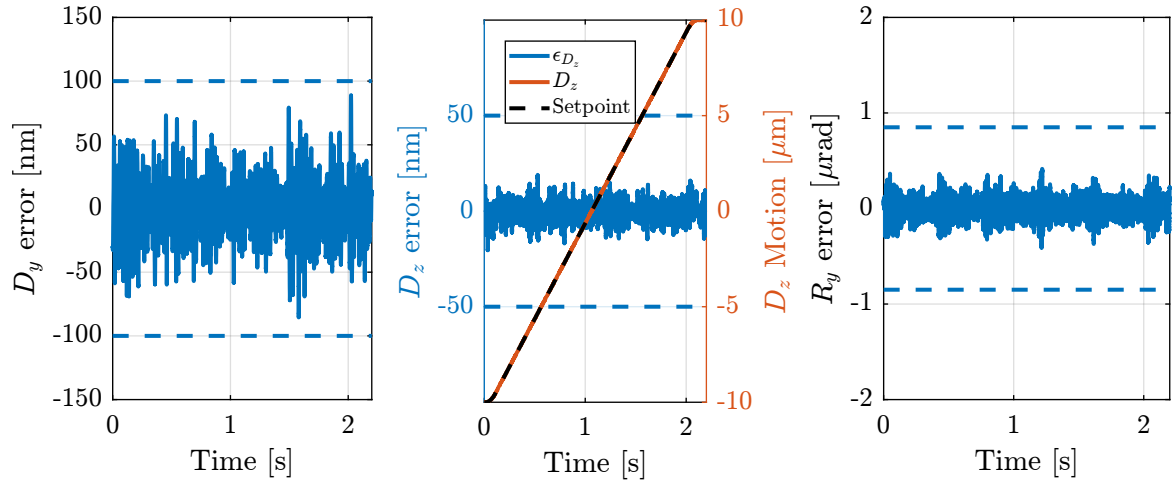

(a) D_y **(b)** D_z **(c)** R_y

Figure 5.7: D_z scan at a velocity of $10\,\mu m/s$. D_z setpoint, measured position and error are shown in (b). Errors in D_y and R_y are respectively shown in (a) and (c)

However, performance during acceleration phases could be enhanced through the implementation of feedforward control.

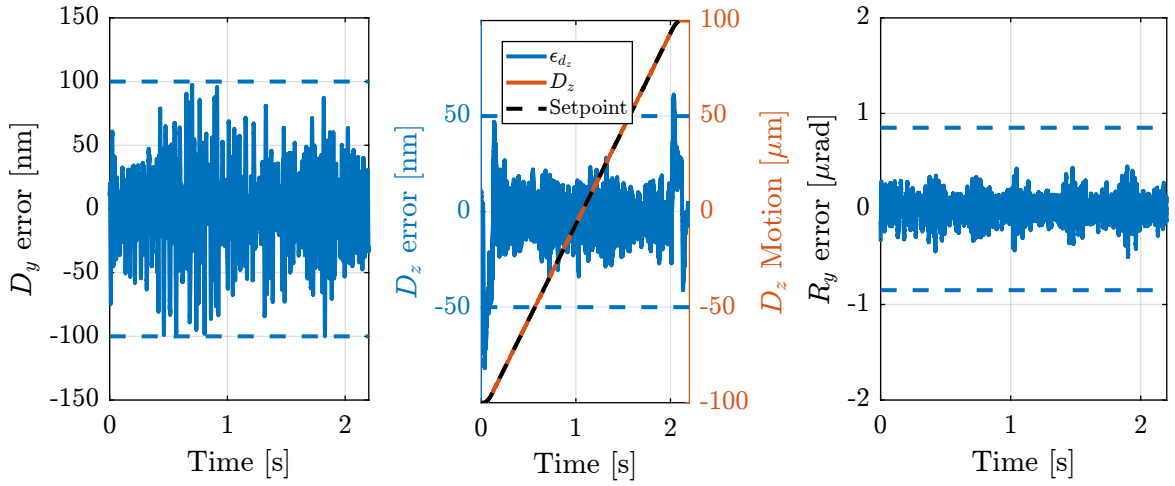

(a) D_y **(b)** D_z **(c)** R_y

Figure 5.8: D_z scan at a velocity of $100\,\mu m/s$. D_z setpoint, measured position and error are shown in (b). Errors in D_y and R_y are respectively shown in (a) and (c)

5.4 Lateral Scans

Lateral scans are executed using the T_y stage. The stepper motor controller[3] generates a setpoint that is transmitted to the Speedgoat. Within the Speedgoat, the system computes the positioning error by comparing the measured D_y sample position against the received setpoint, and the Nano-Hexapod compensates for positioning errors introduced during T_y stage scanning. The scanning range is constrained $\pm 100\,\mu m$ due to the limited acceptance of the metrology system.

Slow scan Initial testing utilized a scanning velocity of $10\,\mu m/s$, which is typical for these experiments. Figure 5.9 compares the positioning errors between open-loop (without NASS) and closed-loop operation. In the scanning direction, open-loop measurements reveal periodic errors (Figure 5.9a) attributable to the T_y stage's stepper motor. These micro-stepping errors, which are inherent to stepper motor operation, occur 200 times per motor rotation with approximately 1 mrad angular error amplitude. Given the T_y stage's lead screw pitch of $2\,mm$, these errors manifest as $10\,\mu m$ periodic oscillations with $\approx 300\,nm$ amplitude, which can indeed be seen in the open-loop measurements (Figure 5.9a).

In the vertical direction (Figure 5.9b), open-loop errors likely stem from metrology measurement error because the top interferometer points at a spherical target surface (see Figure 1.6a). Under closed-loop control, positioning errors remain within specifications in all directions.

Fast Scan The system performance was evaluated at an increased scanning velocity of $100\,\mu m/s$, and the results are presented in Figure 5.10. At this velocity, the micro-stepping errors generate

[3]The "IcePAP" [4] which is developed at the ESRF.

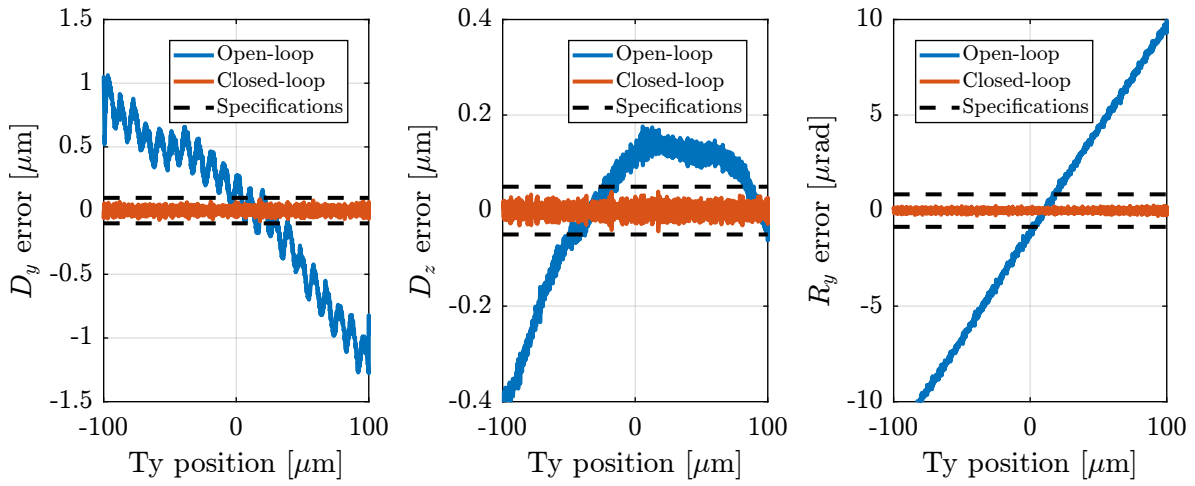

(a) D_y **(b)** D_z **(c)** R_y

Figure 5.9: Open-Loop (in blue) and Closed-loop (i.e. using the NASS, in red) during a 10 $\mu m/s$ scan with the T_y stage. Errors in D_y is shown in (a).

10 Hz vibrations, which are further amplified by micro-station resonances. These vibrations exceeded the NASS feedback controller bandwidth, resulting in limited attenuation under closed-loop control. This limitation exemplifies why stepper motors are suboptimal for "long-stroke/short-stroke" systems requiring precise scanning performance [5].

Two potential solutions exist for improving high-velocity scanning performance. First, the T_y stage's stepper motor could be replaced by a three-phase torque motor. Alternatively, since closed-loop errors in D_z and R_y directions remain within specifications (Figures 5.10b and 5.10c), detector triggering could be based on measured D_y position rather than time or T_y setpoint, reducing sensitivity to D_y vibrations. For applications requiring small D_y scans, the nano-hexapod can be used exclusively, although with limited stroke capability.

5.5 Diffraction Tomography

In diffraction tomography experiments, the micro-station performs combined motions: continuous rotation around the R_z axis while performing lateral scans along D_y. For this validation, the spindle maintained a constant rotational velocity of 6 deg/s while the nano-hexapod performs the lateral scanning motion. To avoid high-frequency vibrations typically induced by the stepper motor, the T_y stage was not utilized, which constrained the scanning range to approximately $\pm 100\,\mu m/s$. The system performance was evaluated at three lateral scanning velocities: $0.1\,mm/s$, $0.5\,mm/s$, and $1\,mm/s$. Figure 5.11 presents both the D_y position setpoints and the corresponding measured D_y positions for all tested velocities.

The positioning errors measured along D_y, D_z, and R_y directions are displayed in Figure 5.12. The system maintained positioning errors within specifications for both D_z and R_y (Figures 5.12b and 5.12c). However, the lateral positioning errors exceeded specifications during the acceleration and deceleration phases (Figure 5.12a). These large errors occurred only during $\approx 20\,ms$ intervals; thus, a delay of $20\,ms$ could be implemented in the detector the avoid integrating the beam when these large errors are

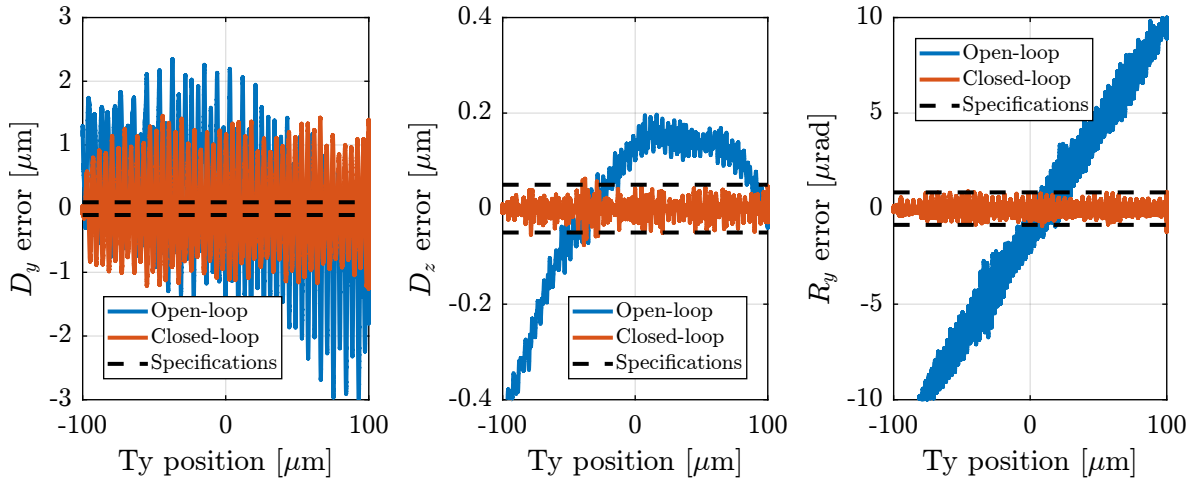

(a) D_y **(b)** D_z **(c)** R_y

Figure 5.10: Open-Loop (in blue) and Closed-loop (i.e. using the NASS, in red) during a 100 $\mu m/s$ scan with the T_y stage. Errors in D_y is shown in (a).

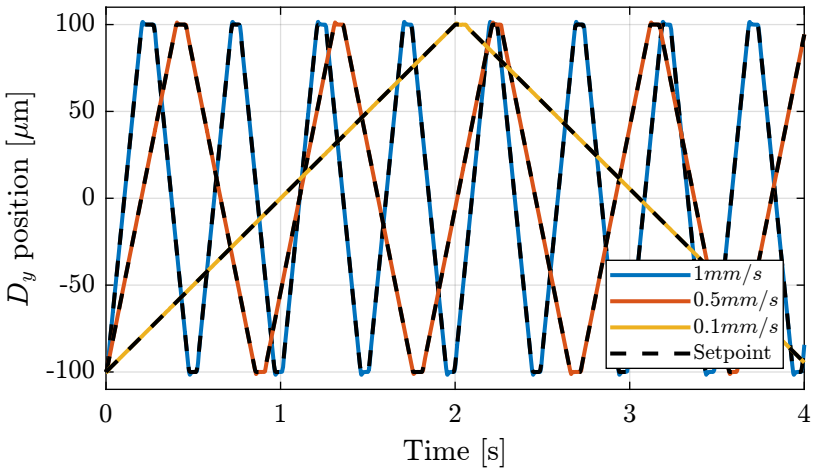

Figure 5.11: Dy motion for several configured velocities

occurring. Alternatively, a feedforward controller could improve the lateral positioning accuracy during these transient phases.

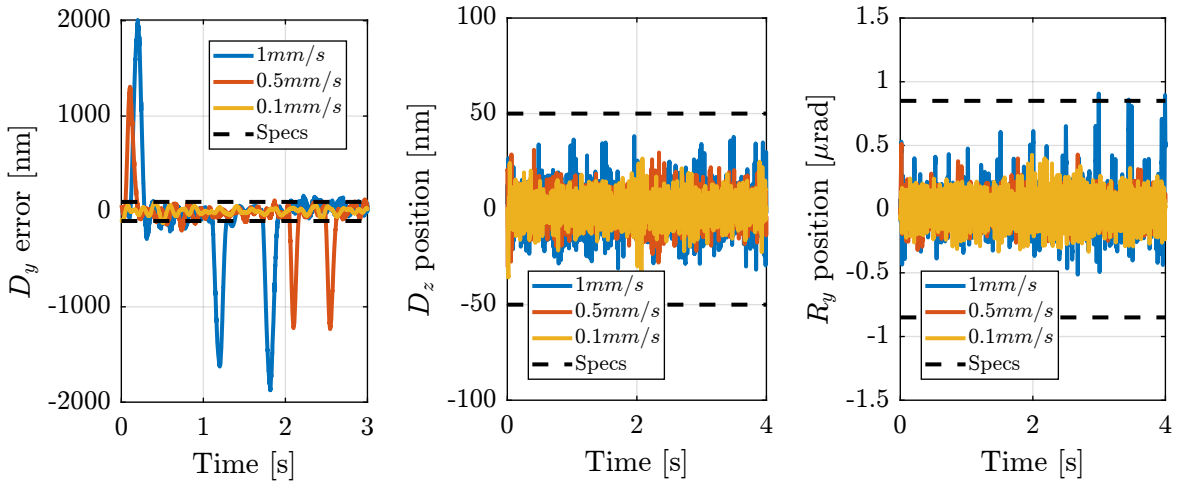

(a) D_y **(b)** D_z **(c)** R_y

Figure 5.12: Diffraction tomography scans (combined R_z and D_y motions) at several D_y velocities (R_z rotational velocity is 6 deg/s).

Conclusion

A comprehensive series of experimental validations was conducted to evaluate the NASS performance over a wide range of typical scientific experiments. The system demonstrated robust performance in most scenarios, with positioning errors generally remaining within specified tolerances (30 nm RMS in D_y, 15 nm RMS in D_z, and 250 nrad RMS in R_y).

For tomography experiments, the NASS successfully maintained good positioning accuracy at rotational velocities up to 180 deg/s with light payloads, though performance degraded somewhat with heavier masses. The HAC-LAC control architecture proved particularly effective, with the decentralized IFF providing damping of nano-hexapod suspension modes, while the high authority controller addressed low-frequency disturbances.

The vertical scanning capabilities were validated in both step-by-step and continuous motion modes. The system successfully resolved 10 nm steps with 50 ms detector integration time, while maintaining positioning accuracy during continuous scans at speeds up to 100 $\mu m/s$.

For lateral scanning, the system performed well at moderate speeds (10 $\mu m/s$) but showed limitations at higher velocities (100 $\mu m/s$) due to stepper motor-induced vibrations in the T_y stage.

The most challenging test case - diffraction tomography combining rotation and lateral scanning - demonstrated the system's ability to maintain vertical and angular stability while highlighting some limitations in lateral positioning during rapid accelerations. These limitations could be addressed through feedforward control or alternative detector triggering strategies.

Overall, the experimental results validate the effectiveness of the developed control architecture and

demonstrate that the NASS meets most design specifications across a wide range of operating conditions (summarized in Table 5.2). The identified limitations, primarily related to high-speed lateral scanning and heavy payload handling, provide clear directions for future improvements.

Table 5.2: Summary of the experimental results performed using the NASS on ID31. Open-loop errors are indicated on the left of the arrows. Closed-loop errors that are outside the specifications are indicated by bold number.

Experiments	D_y **[nmRMS]**	D_z **[nmRMS]**	R_y **[nradRMS]**
Tomography (6 deg/s)	142 ⇒ 15	32 ⇒ 5	464 ⇒ 56
Tomography (6 deg/s, 13kg)	149 ⇒ 25	26 ⇒ 6	471 ⇒ 55
Tomography (6 deg/s, 26kg)	202 ⇒ 25	36 ⇒ 7	1737 ⇒ 104
Tomography (6 deg/s, 39kg)	297 ⇒ **53**	38 ⇒ 9	1737 ⇒ 170
Tomography (180 deg/s)	143 ⇒ **38**	24 ⇒ 11	252 ⇒ 130
Tomography (180 deg/s, custom HAC)	143 ⇒ 29	24 ⇒ 5	252 ⇒ 142
Reflectivity (100 μrad/s)	28	6	118
D_z scan (10 $\mu m/s$)	25	5	108
D_z scan (100 $\mu m/s$)	**35**	9	132
Lateral Scan (10 $\mu m/s$)	585 ⇒ 21	155 ⇒ 10	6300 ⇒ 60
Lateral Scan (100 $\mu m/s$)	1063 ⇒ **732**	167 ⇒ **20**	6445 ⇒ **356**
Diffraction tomography (6 deg/s, 0.1 mm/s)	**36**	7	113
Diffraction tomography (6 deg/s, 0.5 mm/s)	29	8	81
Diffraction tomography (6 deg/s, 1 mm/s)	**53**	10	135
Specifications	30	15	250

Conclusion

This chapter presented a comprehensive experimental validation of the Nano Active Stabilization System (NASS) on the ID31 beamline, demonstrating its capability to maintain precise sample positioning during various experimental scenarios. The implementation and testing followed a systematic approach, beginning with the development of a short-stroke metrology system to measure the sample position, followed by the successful implementation of a HAC-LAC control architecture, and concluding in extensive performance validation across diverse experimental conditions.

The short-stroke metrology system, while designed as a temporary solution, proved effective in providing high-bandwidth and low-noise 5-DoF position measurements. The careful alignment of the fibered interferometers targeting the two reference spheres ensured reliable measurements throughout the testing campaign.

The implementation of the control architecture validated the theoretical framework developed earlier in this project. The decentralized Integral Force Feedback (IFF) controller successfully provided robust damping of suspension modes across all payload conditions (0-39 kg), reducing peak amplitudes by approximately a factor of 10. The High Authority Controller (HAC) effectively rejects low-frequency disturbances, although its performance showed some dependency on payload mass, particularly for lateral motion control.

The experimental validation covered a wide range of scientific scenarios. The system demonstrated remarkable performance under most conditions, meeting the stringent positioning requirements (30 nm RMS in D_y, 15 nm RMS in D_z, and 250 nrad RMS in R_y) for the majority of test cases. Some limitations were identified, particularly in handling heavy payloads during rapid motions and in managing high-speed lateral scanning with the existing stepper motor T_y stage.

The successful validation of the NASS demonstrates that once an accurate online metrology system is developed, it will be ready for integration into actual beamline operations. The system's ability to maintain precise sample positioning across a wide range of experimental conditions, combined with its robust performance and adaptive capabilities, suggests that it will significantly enhance the quality and efficiency of X-ray experiments at ID31. Moreover, the systematic approach to system development and validation, along with a detailed understanding of performance limitations, provides valuable insights for future improvements and potential applications in similar high-precision positioning systems.

Bibliography

[1] J. Watchi, S. Cooper, B. Ding, C. M. Mow-Lowry, and C. Collette, "A review of compact interferometers," *CoRR*, 2018. eprint: 1808.04175 (cit. on p. 9).

[2] R. Hino, P. Fajardo, N. Janvier, T. L. Caër, and F. L. Mentec, "A position encoder processing unit," *Proceedings of the 16th Int. Conf. on Accelerator and Large Experimental Control Systems*, no. nil, Spain, 2018 (cit. on p. 11).

[3] S. Skogestad and I. Postlethwaite, *Multivariable Feedback Control: Analysis and Design - Second Edition*. John Wiley, 2007 (cit. on p. 20).

[4] N. Janvier, J. Clement, P. Fajardo, and G. Cuní, "Icepap: An advanced motor controller for scientific applications in large user facilities," *TUPPC081, ICALEPCS2013, San Francisco*, vol. 2016, 2013 (cit. on p. 31).

[5] T. Dehaeze and L. Ducotté, "The fastjack - a robust, uhv compatible and high performance linear actuator," EUSPEN, 2022 (cit. on p. 32).